Cellular and Molecular Life Sciences (2023) 80:92
https://doi.org/10.1007/s00018-023-04733-8

ORIGINAL ARTICLE

UBE2T resolves transcription-replication conflicts and protects common fragile sites in primordial germ cells

Yongze Yu[1,2,3,4,5,6] · Weiwei Xu[1,2,3,4,5,6] · Canxin Wen[1,2,3,4,5,6] · Simin Zhao[1,2,3,4,5,6] · Guangyu Li[1,2,3,4,5,6] · Ran Liu[1,2,3,4,5,6] · Zi-Jiang Chen[1,2,3,4,5,6,7,8,9] · Yingying Qin[1,2,3,4,5,6] · Jinlong Ma[1,2,3,4,5,6] · Yajuan Yang[1,2,3,4,5,6] · Shidou Zhao[1,2,3,4,5,6]

Received: 2 November 2022 / Revised: 4 February 2023 / Accepted: 22 February 2023 / Published online: 16 March 2023

Abstract

The proper development of primordial germ cells (PGCs) is an essential prerequisite for gametogenesis and mammalian fertility. The Fanconi anemia (FA) pathway functions in maintaining the development of PGCs. FANCT/UBE2T serves as an E2 ubiquitin-conjugating enzyme that ubiquitylates the FANCD2-FANCI complex to activate the FA pathway, but its role in the development of PGCs is not clear. In this study, we found that *Ube2t* knockout mice showed defects in PGC proliferation, leading to severe loss of germ cells after birth. Deletion of UBE2T exacerbated DNA damage and triggered the activation of the p53 pathway. We further demonstrated that UBE2T counteracted transcription-replication conflicts by resolving R-loops and stabilizing replication forks, and also protected common fragile sites by resolving R-loops in large genes and promoting mitotic DNA synthesis to maintain the genome stability of PGCs. Overall, these results provide new insights into the function and regulatory mechanisms of the FA pathway ensuring normal development of PGCs.

Keywords DNA damage response · Replication stress · MiDAS · Fertility

Introduction

Germ cells are responsible for passing genetic information to the offspring and are capable of preserving genome with high stability. Gametogenesis involves two important stages, namely the development of primordial germ cells (PGCs) and the subsequent meiosis, and any genome instability during these processes will impair the quantity or quality of germ cells and reproductive potential of mammals [1]. DNA damage response (DDR) mechanisms have been well illustrated to ensure genome stability during meiosis [2–4], but much less is known about how genome stability is maintained in rapid proliferating PGCs. The Fanconi anemia (FA) pathway serving as a classical DDR pathway is indispensable for the maintenance of reproductive capacity of both sexes [5]. The reduced fertility and massive loss of germ

✉ Jinlong Ma
majinlong123@hotmail.com

✉ Yajuan Yang
yangyajuan1991@163.com

✉ Shidou Zhao
shidouzhao@sdu.edu.cn

1 Center for Reproductive Medicine, Shandong University, Jinan 250012, Shandong, China

2 Key Laboratory of Reproductive Endocrinology of Ministry of Education, Shandong University, Jinan 250012, Shandong, China

3 Shandong Key Laboratory of Reproductive Medicine, Jinan 250012, Shandong, China

4 Shandong Provincial Clinical Research Center for Reproductive Health, Jinan 250012, Shandong, China

5 Shandong Technology Innovation Center for Reproductive Health, Jinan 250012, Shandong, China

6 National Research Center for Assisted Reproductive Technology and Reproductive Genetics, Shandong University, Jinan 250012, Shandong, China

7 Research Unit of Gametogenesis and Health of ART-Offspring, Chinese Academy of Medical Sciences, Jinan 250021, Shandong, China

8 Shanghai Key Laboratory for Assisted Reproduction and Reproductive Genetics, Shanghai 200135, China

9 Center for Reproductive Medicine, School of Medicine, Ren Ji Hospital, Shanghai Jiao Tong University, Shanghai 200135, China

cells observed in FA patients and null mice have been attributed to defects in PGC proliferation and meiosis [5]. Previous studies have shown that PGC loss in FA gene mutant mice is mainly due to increased DNA damage that activates the p53 pathway [6, 7]. However, the source of DNA damage in FA pathway-deficient PGCs needs to be determined.

Up to now, mutations in 22 FA genes (*FANCA–W*) have been identified to cause FA, a rare genetic disorder manifested as progressive bone marrow failure, somatic malformations, a high predisposition to cancers, and reduced fertility [8]. The FA pathway is responsible for repair of DNA inter-strand crosslinks (ICLs) in which the FA core complex recognizes the ICL site, then FANCD2-FANCI (ID2) complex is monoubiquitylated and recruits downstream repair factors to complete repair [8, 9]. In addition, the FA pathway also protects replication forks (RFs) under replication stress that refers to any process slowing or stalling the RFs [10–13]. Transcription-replication conflicts (TRCs) cause endogenous replication stress by inducing RF stalling and thus exposing the single-stranded DNA (ssDNA) [14]. The ID2 complex and FANCM are both present at stalled RFs [8] and may protect the nascent DNA strands by binding to the ssDNA and inhibiting MRE11mediated DNA resection [8, 15, 16]. On the other hand, TRCs also promote the formation of DNA:RNA hybrids (R-loops) [14, 17], and the removal of R-loops by the FA pathway is crucial for avoiding DNA damage [18, 19].

Furthermore, the FA pathway is also involved in the protection of common fragile sites (CFSs), which are large chromosomal regions that are prone to forming breaks or gaps under conditions of replication stress [20]. Notably, CFSs, which often co-localize with very large genes longer than 300 kb [21], are another source of endogenous replication stress due to the small number of replication origins and a tendency for R-loop formation in these regions [22, 23]. It is known that a large panel of CFSs remain incompletely duplicated up to early mitosis [24, 25]. These regions undergo a break-induced replication (BIR) process known as mitotic DNA synthesis (MiDAS), showing as the breaks or gaps in metaphase chromosomes and formation of the normal daughter cells [25–27]. If MiDAS doesn't work and existence of incompletely duplicated loci at CFSs continue into late mitosis, ultra-fine bridges (UFBs) between two sister chromatids form [28], and persistent UFBs break, thus generating 53BP1 nuclear bodies (53BP1-NBs) and micronuclei in daughter cells at the G1 phase [29, 30]. The FA pathway is found to facilitate MiDAS of CFSs and thus suppress CFS-related damage [31], but the mechanism remains largely unknown.

E2 ubiquitin conjugating enzyme T (UBE2T), also known as FANCT, is a key component of the FA pathway, and it collaborates with the E3 ubiquitin ligase FANCL to catalyze the ubiquitination of the ID2 complex [32, 33]. However, its function in reproduction has not been determined. In this study, we find that *Ube2t* knockout mice have FA pathway inactivation and proliferation defects in PGCs during embryo development. Mechanistically, the FA pathway deficiency causes the endogenous DNA damage which is derived from unsolved TRCs and incompletely replicated CFSs in PGCs, ultimately leading to insufficient reproductive reserve and infertility.

Results

Deletion of UBE2T causes germ cell loss in mice after birth

To explore the role of UBE2T in mammalian germ cells, we generated *Ube2t* knockout (*Ube2t*$^{-/-}$) mice using the CRISPR/Cas9 technique. Deletion of the targeting sequence caused a frameshift mutation, leading to the premature stop of UBE2T protein (Fig. S1a). The genotype of *Ube2t*$^{-/-}$ mice was validated by PCR (Fig. S1b), and the loss of UBE2T protein in *Ube2t*$^{-/-}$ testes was confirmed by Western blotting (Fig.S1c).

Ube2t$^{-/-}$ mice were viable and were born at the expected Mendelian ratio (Fig. S2a). Both male and female *Ube2t*$^{-/-}$ mice developed normally without obvious defects or body weight differences (Fig. S2b, c). The ovaries of 2-month-old *Ube2t*$^{-/-}$ mice were smaller in size and lower in weight than those of wild-type mice (Fig. S3a, b). Similarly, 3-month-old male *Ube2t*$^{-/-}$ mice had smaller and lower weight testes in comparison to wild-type mice (Fig. S3c, d). Histological analysis showed that ovaries from postnatal day (PD) 3, PD21 and adult female *Ube2t*$^{-/-}$ mice were small and devoid of follicles (Fig. 1a; Fig. S3e). Meanwhile, all of the testes from PD3, PD35, and adult male mice showed a mosaic pattern and most tubules lacked germ cells (Fig. 1b; Fig. S3f). Although no significant differences in the estradiol level were seen between *Ube2t*$^{-/-}$ and wild-type female mice, *Ube2t*$^{-/-}$ female mice had higher serum FSH levels (2.20 ± 0.97 mIU/ml vs. 1.31 ± 0.48 mIU/ml, $P = 0.021$) and had no estrous cycles (Fig. S2d-f). Because both male and female mice exhibited severe reductions in germ cells at PD3, we speculated that germ cell loss might start in the embryonic period.

UBE2T is critical for the development of mouse PGCs

To identify the stage at which the loss of germs cells started, we used immunofluorescence staining of DDX4, a germ cell marker, together with the pre-granulosa cell marker FOXL2 or the Sertoli cell marker SOX9 to detect germ cells at embryonic day 13.5 (E13.5) and E15.5. Both female and male *Ube2t*$^{-/-}$ embryonic gonads showed severely decreased

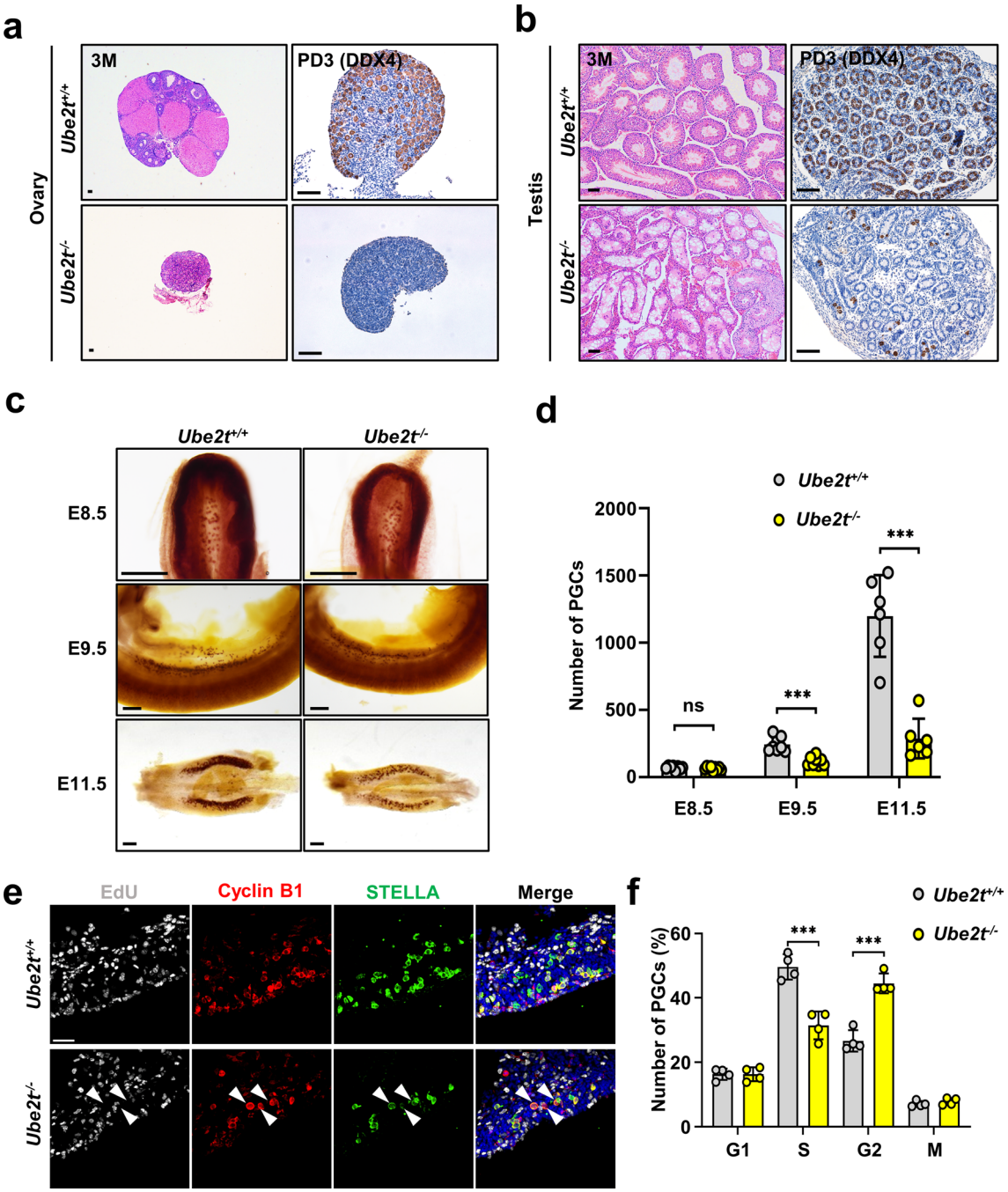

Fig. 1 Proliferation defects of *Ube2t*$^{-/-}$ PGCs lead to profound germ cells loss **a** H&E and immunohistochemical staining for DDX4 (a germ cell marker, brown) in the ovaries at PD3 and 3 months. Scale bars = 50 µm. **b** H&E and immunohistochemical staining for DDX4 (brown) of testes at PD3 and 3 months. Scale bars = 50 µm. **c, d** Representative images (**c**) and quantification (**d**) of wild-type and *Ube2t*$^{-/-}$ PGCs using alkaline phosphatase staining of E8.5 embryos, E9.5 embryos, and E11.5 genital ridges. Scale bars = 200 µm. Data from individual embryos are presented as dots and mean ± SD are presented, $n = 8/9/8/8/6/6$ embryos, ns: not significant, $^{***}P < 0.001$. **e, f** Representative images (**e**) and percentages (**f**) of the cell cycle distribution of PGCs in E11.5 wild-type and *Ube2t*$^{-/-}$ genital ridges. G1-phase cells, cyclin B1 negative; S-phase cells, EdU positive; G2-phase cells, cyclin B1 strongly positive in cytoplasm; M-phase cells, cyclin B1 accumulation in the nucleus. STELLA-positive indicates PGC, and arrowheads indicate G2-phase PGCs. $n = 4$ embryos per genotype, $^{***}P < 0.001$. Scale bar = 50 µm. Data from individual embryos are presented as dots and mean ± SD are presented

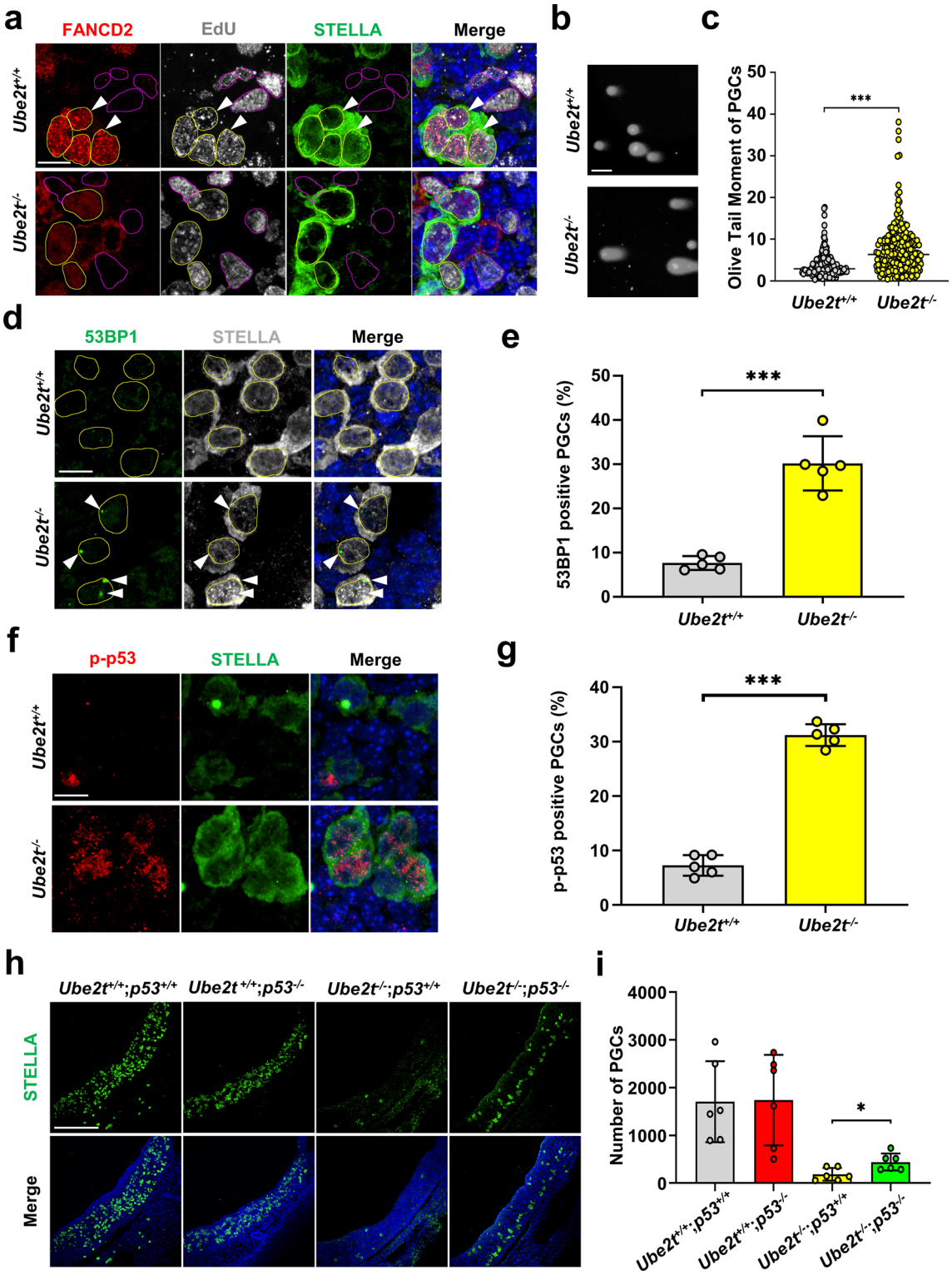

numbers of germ cells compared with wild-type embryos (Fig. S4a, b). Because female germ cells begin to enter meiosis at E13.5 and male germ cells arrest at the G1/G0 phase of mitosis after E14.5 [34], these results indicate that *Ube2t*$^{-/-}$ embryonic germ cells are lost prior to meiosis.

Previous studies have revealed that many FA-null mouse models have severely reduced numbers of PGCs [35], so we used alkaline phosphatase staining to detect PGCs in mouse embryos at E8.5, E9.5, and E11.5. While no significant difference was found between the PGC numbers of

◂**Fig. 2** Loss of UBE2T leads to DNA damage accumulation and p53 signaling activation in PGCs **a** Immunofluorescence staining for FANCD2 (red), EdU (white), and STELLA (green) to assess FA pathway activation in E11.5 wild-type and *Ube2t*$^{-/-}$ genital ridges. The nuclei of S-phase PGCs and S-phase somatic cells are circled out. Arrowheads indicate FANCD2 foci in PGCs. Scale bar = 10 μm. **b** Representative images of the neutral comet assay for E11.5 wild-type and *Ube2t*$^{-/-}$ PGCs. DNA was stained with Hoechst 33342 (white). Scale bar = 50 μm. **c** Quantification of the OTM in the PGC neutral comet assay. At least 200 PGCs were included per group, ***$P < 0.001$. **d, e** Representative images (**d**) and percentages (**e**) of 53BP1 foci (green) in PGCs (STELLA-positive) in E11.5 wild-type and *Ube2t*$^{-/-}$ genital ridges. The nuclei of PGCs are circled out. Arrowheads indicate 53BP1 foci in PGCs. $n = 5$ embryos per genotype, ***$P < 0.001$. Scale bar = 10 μm. **f, g** Representative images (**f**) and percentages (**g**) for p-p53–positive (red) PGCs (STELLA-positive) in E11.5 wild-type and *Ube2t*$^{-/-}$ genital ridges. $n = 5$ embryos per genotype, ***$P < 0.001$. Scale bar = 10 μm. **h, i** Representative images (**h**) and quantification (**i**) of PGCs (STELLA-positive) in E11.5 genital ridges of the indicated genotypes. $n = 6$ embryos per genotype, *$P < 0.05$. Scale bar = 200 μm. Data from individual cells (**c**) or embryos (**e, g, i**) are presented as dots, mean values (**c**) or mean ± SD (**e, g, i**) are presented

Ube2t$^{-/-}$ and wild-type mice at E8.5, about 48.3% of the PGCs in *Ube2t*$^{-/-}$ embryos remained at E9.5 compared to wild-type (117.1 ± 33.1 vs. 242.6 ± 53.7) and 23.9% remained at E11.5 (286.5 ± 148.0 vs. 1198.0 ± 304.2), respectively (Fig. 1c, d). Meanwhile, the similar distribution pattern of *Ube2t*$^{-/-}$ and wild-type PGCs from E8.5 to E11.5 indicated that UBE2T did not play a major role in PGC migration. These results indicate that PGCs are specified normally, but their expansion may be defective upon UBE2T deficiency.

Loss of UBE2T leads to proliferation defects in mouse PGCs

To determine the cause for the reduced number of PGCs, we examined key events in the development of PGCs. OCT-4, a pluripotency marker was used to detect the pluripotency of PGCs, and no obvious differences were found in *Ube2t*$^{-/-}$ and wild-type E11.5 PGCs (Fig. S5a). We then checked if the epigenetic reprogramming process was affected. The key epigenetic modifications, including 5-methylcytosine (5mC), histone H3 lysine 9 dimethylation (H3K9me2), and histone H3 lysine 27 trimethylation (H3K27me3), were removed or established normally in E11.5 *Ube2t*$^{-/-}$ PGCs (Fig. S5b-d). We next examined cell cycle progression and apoptosis in PGCs. Increased apoptosis was seen in *Ube2t*$^{-/-}$ PGCs compared with wild-type PGCs (2.07 ± 0.98% vs. 0.41 ± 0.16%, $P = 0.016$), as indicated by Cleaved-PARP1 staining (Fig. S6a, b). However, the overall apoptosis rate in *Ube2t*$^{-/-}$ PGCs was really low, suggesting that apoptosis may not be the major cause of PGCs loss. In addition, almost all PGCs were positive for Ki67 staining in both *Ube2t*$^{-/-}$ and wild-type PGCs (Fig. S6c, d), suggesting that almost all PGCs were actively progressing through the cell cycle. Furthermore, Cyclin B1 staining together with 5-ethynyl-2'-deoxyuridine (EdU) incorporation was used to determine the cell cycle progression of PGCs. While the percentage of *Ube2t*$^{-/-}$ PGCs in S phase was reduced compared to that of wild-type PGCs (31.46 ± 4.33% vs. 49.63 ± 3.94%, $P < 0.001$), the percentage of *Ube2t*$^{-/-}$ PGCs in G2 phase was 1.67-fold greater than in wild-type PGCs (44.49 ± 3.07% vs. 26.67 ± 3.33%, $P < 0.001$). Comparable results were found for the percentages of both G1-phase and M-phase cells between *Ube2t*$^{-/-}$ and wild-type PGCs (Fig. 1e, f). Together, these results suggest that UBE2T is vital for the rapid expansion of PGCs and that UBE2T deficiency leads to proliferation defects of PGCs.

To perform functional validation in vitro, we used the P19 cell line, which was isolated from a mouse teratocarcinoma and exhibited the biochemical features of PGCs [36]. The PGC markers PRDM1 and STELLA were clearly detected in P19 cells, but not in mouse embryonic fibroblasts (MEFs) (Fig. S7a). In addition, the expression of UBE2T and FANCD2 in P19 cells was higher than that in MEFs (Fig. S7a). These findings indicate that P19 is a PGC-like cell line that possesses high FA pathway activity. For in vitro experiments, we knocked down UBE2T by adenovirus infection in P19 cells, and UBE2T was almost completely absent (Fig. S7b). Following *Ube2t* knockdown, ubiquitinated FANCD2 was also almost undetectable in P19 cells (Fig. S7b). The percentage of P19 cells in S phase was reduced compared to that of control cells, and *Ube2t* knockdown in P19 cells caused an increase in the proportion of cells in G2 phase compared to control cells (Fig. S7c). These results provide in vitro evidence that UBE2T deficiency causes PGC proliferation defects.

UBE2T deficiency causes DNA damage accumulation and p53 signalling activation in PGCs

Next, we tested whether UBE2T was necessary for the activation of the FA pathway in vivo. Our results showed that FANCD2 foci, which are an indicator of FA pathway activation, were clearly formed in the nuclei in wild-type S-phase PGCs but were absent in *Ube2t*$^{-/-}$ PGCs (Fig. 2a). In addition, we noticed that FANCD2 was almost invisible in surrounding S-phase somatic cells, indicating that the functional FA pathway played a more important role in the development of PGCs (Fig. 2a). We next separated wild-type and *Ube2t*$^{-/-}$ MEFs from mouse embryos and cultured them in vitro. Western blotting showed that after treatment with MMC or aphidicolin (APH) to induce ICLs and replication stress, respectively, a high-level of ubiquitinated FANCD2 was detected in wild-type MEFs but not in *Ube2t*$^{-/-}$ MEFs

(Fig. S7d). These findings suggest that UBE2T deficiency causes FA pathway inactivation.

We then isolated PGCs from E11.5 genital ridges using magnetic sorting and performed a neutral comet assay to quantify the extent of the DNA damage. The average olive tail moment (OTM) of *Ube2t*$^{-/-}$ PGCs was significantly increased compared to wild-type PGCs (7.62 ± 6.03 vs. 3.66 ± 2.73, $P < 0.0001$) (Fig. 2b, c). Moreover, the percentage of 53BP1-positive *Ube2t*$^{-/-}$ PGCs was increased 3.95-fold compared to wild-type PGCs ($30.20 \pm 6.13\%$ vs. $7.65 \pm 1.60\%$, $P < 0.0001$) (Fig. 2d, e). Similarly, the OTM and the percentage of cells with > 5 53BP1 foci in *Ube2t* knockdown P19 cells were both increased compared with those in control cells (Fig. S7e, f, h, i). Similar results were found in *Ube2t*$^{-/-}$ MEFs when inducing replication stress by APH or hydroxyurea (HU) and inducing ICLs by MMC (Fig. S7g, j). Furthermore, following MMC or APH treatment western blotting showed that γH2AX expression was increased in *Ube2t*$^{-/-}$ MEFs (Fig. S7d). Taken together, these results confirm that UBE2T deficiency causes DNA damage accumulation in PGCs.

It is well known that p53 is a transcription factor and functions as a sensor of DNA damage to control cell cycle progression and regulate apoptosis [37]. Previous studies showed that p53 played a major role in slowing cell cycle progression in FA cells [38], and our results showed that the proportion of phosphorylated p53 (p-p53)-positive *Ube2t*$^{-/-}$ PGCs was significantly increased compared to wild-type PGCs ($31.22 \pm 2.00\%$ vs. $7.25 \pm 1.89\%$, $P < 0.0001$) (Fig. 2f, g). Western blotting also showed increased expression of p-p53 in *Ube2t*$^{-/-}$ MEFs following MMC or APH treatment (Fig. S7d). After double knockout of *Ube2t* and *p53*, the number of E11.5 PGCs was partially rescued compared to that of *Ube2t*$^{-/-}$*/p53*$^{+/+}$ mice (442.83 ± 178.54 vs. 185.83 ± 133.38, $P < 0.05$) (Fig. 2h, i). These results support the hypothesis that DNA damage in PGCs caused by UBE2T deficiency triggers p53 pathway activation to slow the cell cycle, leading to PGC proliferation defects.

UBE2T counteracts TRCs by resolving R-loops and protecting RFs

Because UBE2T deletion increased DNA damage in PGCs, we sought to determine the source of the DNA damage. Considering that PGCs are characterized by high levels of transcription and replication [39, 40], we hypothesized that the endogenous replication stress induced by TRCs was one source of DNA damage. To assess the TRC level in PGCs, a proximity-ligation assay (PLA) was performed between RNA polymerase II (Pol II) and PCNA, which indicated the transcription and replication process, respectively. The number of PLA foci was significantly increased upon UBE2T deficiency in PGCs compared to wild-type (Fig. 3a, b), and a similar result was seen in MEF cells (Fig. 4a, b). These results indicate that unresolved TRCs may be the source of replication stress in UBE2T deficient PGCs that lead to DNA damage.

Recent studies suggest that TRCs induce R-loop formation and genomic instability [41] and that removal of R-loops by the FA pathway is crucial for counteracting TRCs and avoiding DNA damage [18, 19]. We measured the formation of R-loops by staining with the S9.6 antibody that recognizes DNA:RNA hybrids. Depletion of UBE2T increased the intensity of the S9.6 signal in PGCs (Fig. 3c, d), whereas no obvious differences in the transcription levels in *Ube2t*$^{-/-}$ and wild-type PGCs were detected (Fig. S6e), indicating that the increased R-loops and TRCs in *Ube2t*$^{-/-}$ PGCs were not due to global transcriptional changes. We also observed an increased S9.6 signal in *Ube2t*$^{-/-}$ MEFs compared to wild-type MEFs (Fig. 4c, d). We next found that the elevated S9.6 signal intensity was significantly reduced by overexpression of RNase H1 (RNH1), which is an R-loop-specific nuclease, in *Ube2t*$^{-/-}$ MEFs (Fig. 4c, d). The PLA signal was also significantly reduced after RNH1 overexpression in *Ube2t*$^{-/-}$ MEFs (Fig. 4a, b). To directly confirm the role of UBE2T in R-loop resolution, we used S9.6 antibody to detect R-loop sites by using the CUT&Tag assay in P19 cells. We found that R-loops were enriched at transcription start sites (TSSs) and were mainly located at the promoter regions (Fig. 5a, b; Fig. S8a), and the R-loop signals were significantly increased at TSSs and promoter regions in *Ube2t* knockdown P19 cells (Fig. 5b). Comparative analysis showed that most R-loop peaks in control group were shared with *Ube2t* knockdown groups, and the *Ube2t* knockdown groups showed more sh*Ube2t*-only R-loop peaks (Fig. 5c). Further analysis of the sh*Ube2t*-only peaks and the shared peaks showed that *Ube2t* knockdown groups exhibited higher R-loop signals than those in control group in each peak region (Fig. 5d, e; Fig. S8b, c), indicating the significant accumulation of R-loops upon *Ube2t* knockdown. Two representative genes, *Rapgef6* and *Taf15*, were displayed (Fig. 5f). To evaluate the effect of R-loops on RF velocity, we infected MEFs with exogenous RNH1 and pulse-labeled nascent DNA with the nucleotide analogues iododeoxyuridine (IdU) and chlorodeoxyuridine (CldU) and performed the DNA fiber assay. Depletion of UBE2T in MEFs caused reduced RF velocity, as shown by shorter CldU track lengths, and the RF velocity was rescued by the overexpression of RNH1 (Fig. 4e). These results demonstrate that UBE2T deficiency causes the accumulation of R-loops, especially at promoter regions, which act as obstacles to the progression of RFs and exacerbate the generation of TRCs.

R-loops cause RFs to progress slowly or even stall, and in such cases the exposed ssDNA can be cleaved by nucleases [42, 43]. Previous studies showed that FANCD2 could bind to the ssDNA of stalled RFs and protect the nascent

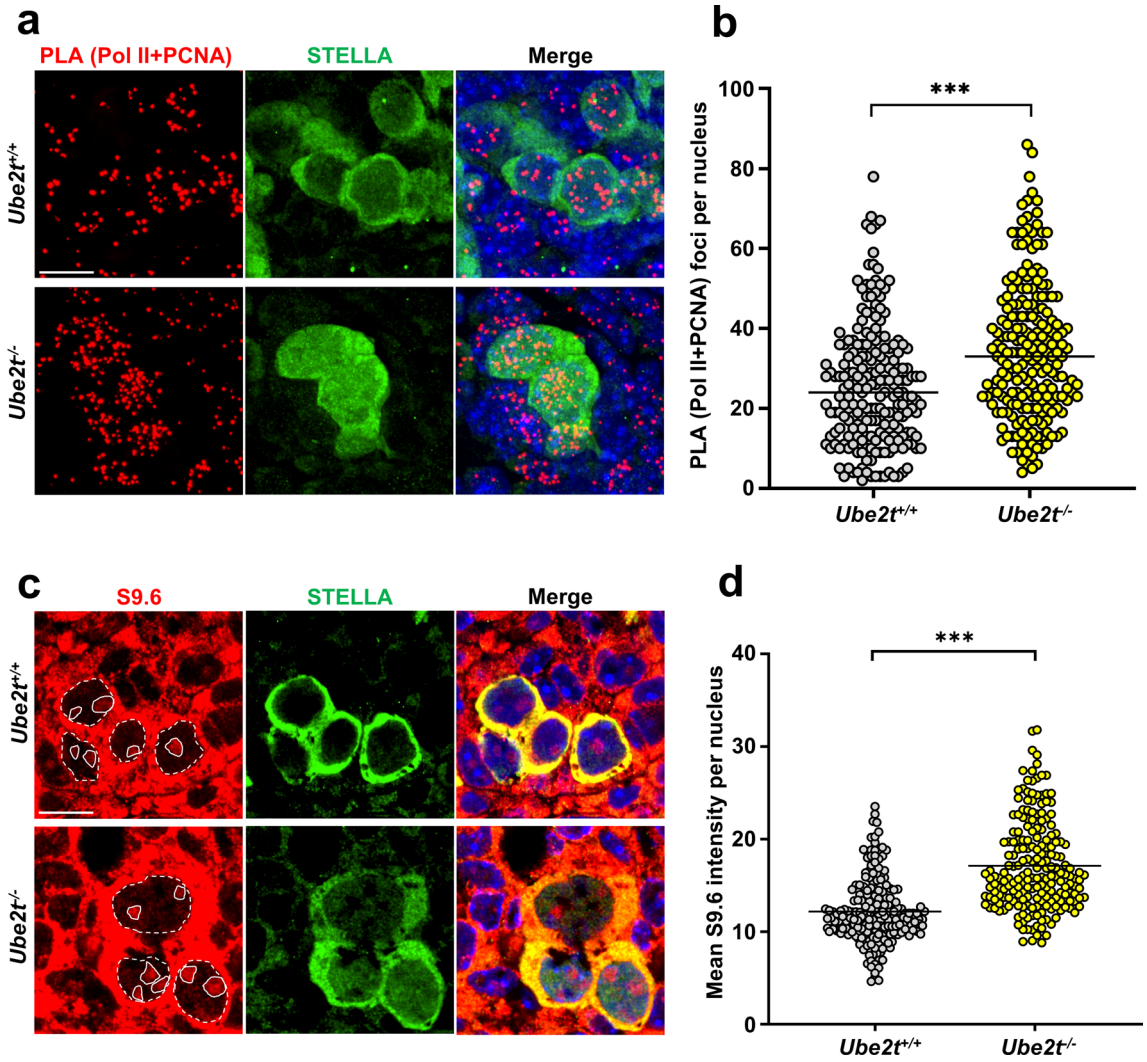

Fig. 3 Loss of UBE2T leads to R-loop and TRC accumulation in PGCs **a, b** Representative images (**a**) and quantification (**b**) of TRCs in PGCs (STELLA-positive) in E11.5 wild-type and *Ube2t*$^{-/-}$ genital ridges. PLA (Pol II + PCNA) foci (red) indicate TRCs. At least 200 PGCs were included per genotype, ***$P < 0.001$. Scale bar = 10 μm. **c, d** Representative images (**c**) and quantification (**d**) of R-loops in PGCs (STELLA-positive) in E11.5 wild-type and *Ube2t*$^{-/-}$ genital ridges. The mean S9.6 intensity (red) in the nucleus after subtracting the nucleolar signal indicates the level of R-loops. At least 200 PGCs were included per genotype, ***$P < 0.001$. Scale bar = 10 μm. Data from individual cells are presented as dots and the mean values are presented (**b, d**)

DNA from being degraded by MRE11 [15, 16]. To assess the role of UBE2T in the protection of stalled RFs, we treated P19 cells and MEFs with HU or APH after IdU and CldU labelling and then performed the DNA fiber assay. Our results showed that treating *Ube2t* knockdown P19 cells and *Ube2t*$^{-/-}$ MEFs with APH or HU decreased the CldU:IdU ratios (Fig. 6a–d), thus reflecting the greater resection of nascent DNA. Furthermore, we found that the decreased CldU:IdU ratios in *Ube2t*$^{-/-}$ MEFs were rescued by mirin, a MRE11 inhibitor (Fig. 6c, d), indicating that the resection of nascent DNA was mainly mediated by MRE11. Taken together, these results suggest that UBE2T can counteract TRCs by resolving R-loops and by stabilizing the RF to prevent genomic instability in PGCs.

UBE2T protects the stability of CFSs

CFSs are another source of endogenous replication stress mainly due to their small number of replication origins [22], and the FA pathway is involved in the repair of damaged DNA in mitosis deriving from CFSs [28, 44]. To evaluate the role of UBE2T in protecting CFSs, we examined CFS-related DNA damage in *Ube2t*$^{-/-}$ PGCs and in vitro cell lines. The percentage of 53BP1-NB-positive G1 cells

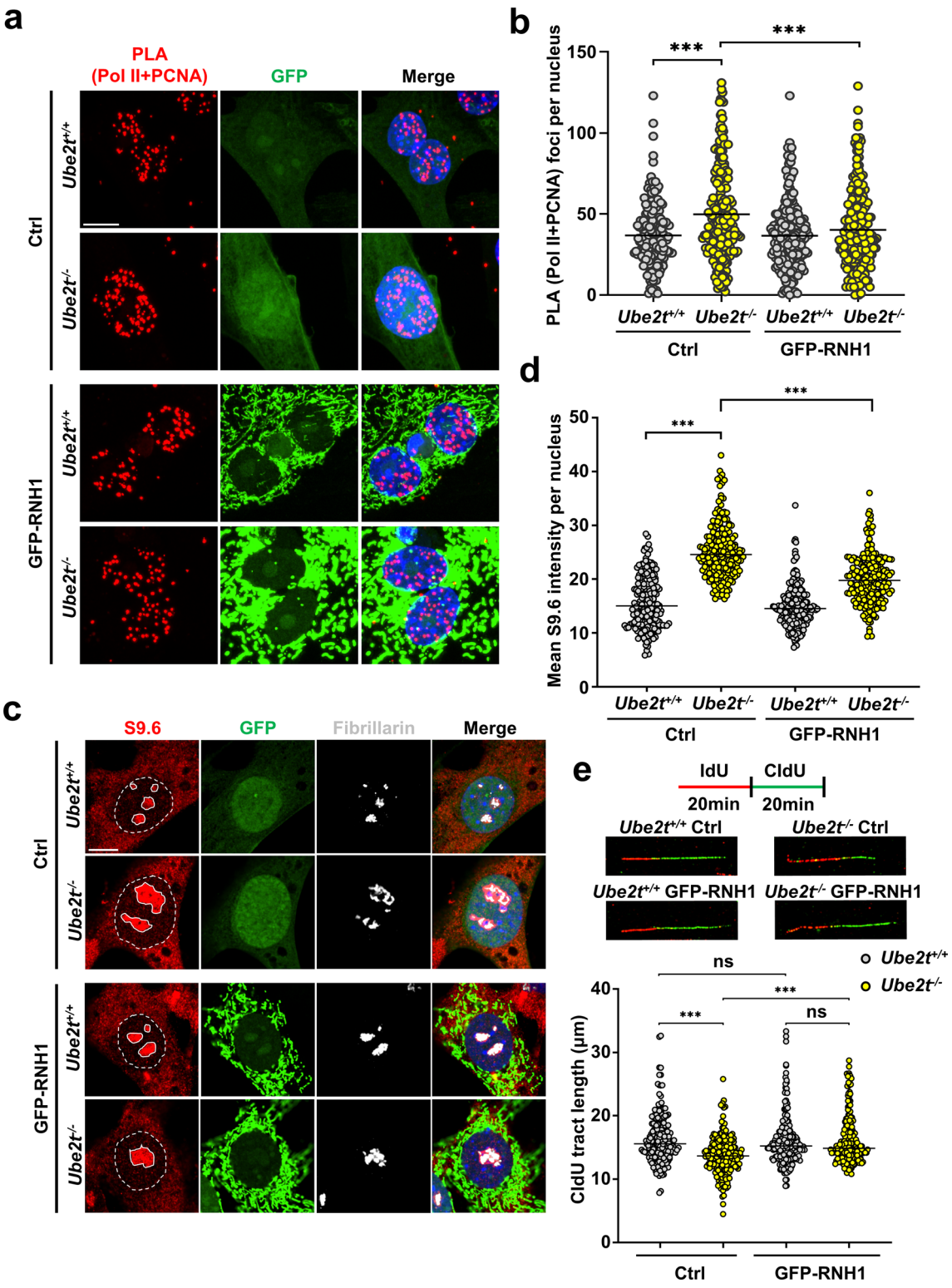

was significantly increased in *Ube2t*$^{-/-}$ PGCs compared to wild-type PGCs (14.03 ± 3.83% vs. 3.14 ± 1.69%, $P < 0.001$) (Fig. 7a, b). Similarly, we also observed a higher percentage of G1 MEFs with 53BP1-NBs with or without APH treatment upon UBE2T deletion (Fig. S9a, b). We then treated MEFs with cytochalasin B to induce the production of binucleated cells. Compared to wild-type MEFs, an increasing number of binucleated *Ube2t*$^{-/-}$ MEFs showed micronuclei regardless of APH treatment (Fig. 7c, d). Given that UFBs were the main cause of micronuclei and 53BP1-NBs

◂**Fig. 4** Loss of UBE2T contributes to R-loop and TRC accumulation in MEFs **a, b** Representative images (**a**) and quantification (**b**) of R-loops of wild-type and *Ube2t*$^{-/-}$ MEFs overexpressing control (green) or GFP-RNaseH1 (GFP-RNH1, green) adenovirus. The mean S9.6 intensity (red) in the nucleus (except the nucleolar signal that is positive for Fibrillarin staining) indicates the number of R-loops. At least 200 MEFs were included per group, ***$P < 0.001$. Scale bar = 10 μm. **c, d** Representative images (**c**) and quantification (**d**) of TRCs in wild-type and *Ube2t*$^{-/-}$ MEFs overexpressing control (green) or GFP-RNH1 (green) adenovirus. PLA (Pol II + PCNA) foci (red) indicate TRCs. At least 200 MEFs were included per group, ***$P < 0.001$. Scale bar = 10 μm. (**e**) Top: The experimental scheme of the DNA fiber assay in MEFs to assess the velocity of RFs. Middle: Representative images of the DNA fiber assay in MEFs. Bottom: CldU track length of the DNA fiber assay in wild-type and *Ube2t*$^{-/-}$ MEFs overexpressing control or GFP-RNH1 adenovirus. At least 200 CldU tracks were included per group, ns: not significant, ***$P < 0.001$. Data from individual cells (**b, d**) or DNA fibers (**E**) are presented as dots, means are presented (**b, d, e**)

in daughter cells, we measured the frequency of UFBs in UBE2T-deficient cells. To obtain more anaphase cells, we treated the P19 cells with nocodazole to synchronize the cells at G2/M phase and then released the cells into anaphase (Fig. 7e). We then performed immunofluorescence staining of PLK1interacting checkpoint helicase (PICH), which labelled CFS-related UFBs [28], in the synchronized P19 cells. We observed more UFBs in *Ube2t* knockdown P19 cells compared to control cells (Fig. 7f, g), and the percentage of *Ube2t*$^{-/-}$ MEFs with UFBs was significantly increased compared to wild-type MEFs with or without APH treatment (Fig. S9c, d). Taken together, these results suggest that UBE2T is essential for maintaining the stability of CFSs.

UBE2T promotes MiDAS by recruiting MUS81 to chromatin

After the under-replicated CFS regions enter mitosis, DNA synthesis will continue in these regions, which is referred to as MiDAS [25, 26]. MiDAS is a rescue pathway for the under-replicated regions of CFSs during mitosis, and is associated with the appearance of UFBs and 53BP1-NBs or micronuclei [25]. To determine the role of UBE2T in MiDAS, we first synchronized the *Ube2t* knockdown P19 cells with RO-3306 at G2 phase and then released the cells to prometaphase along with EdU incorporation (Fig. 8a). We found a significant reduction in the EdU-positive foci per prometaphase P19 cell upon *Ube2t* knockdown, which indicated a low level of MiDAS (Fig. 8b, c). In addition, we also observed a significantly decreased MiDAS signal in *Ube2t*$^{-/-}$ MEFs compared to wild-type MEFs (Fig. 8d). These results suggest that UBE2T facilitates MiDAS.

MiDAS is a BIR process and mainly dependent on MUS81 endonuclease to generate fragile site breakage and on the non-catalytic subunit of the Pol-delta complex (POLD3) to complete DNA synthesis [26, 45]. Considering that MUS81 was downstream of the FA pathway and that ubiquitination of the ID2 complex supported MUS81 recruitment to the chromatin [8], we evaluated whether UBE2T influenced MUS81 recruitment to chromatin and subsequent POLD3-induced DNA synthesis in this BIR process. We extracted the chromatin-bound proteins from asynchronous, G2-arrested, and prometaphase P19 cells and found that knockdown of UBE2T caused an obvious decrease in ubiquitylated FANCD2, MUS81, and POLD3 expression in the chromatin-bound fraction of prometaphase P19 cells (Fig. 8e). To further assess the function of UBE2T in MiDAS, we performed metaphase spreads using the synchronized MEFs under replication stress induced by APH (Fig. 8f). A significant reduction in the number of breaks and gaps in metaphase chromosomes was found in *Ube2t*$^{-/-}$ MEFs (Fig. 8g, h). These findings show that UBE2T deficiency causes FA pathway inactivation, reduces MUS81 recruitment, and restricts MiDAS. Taken together, these results suggest that UBE2T is crucial for MiDAS by recruiting MUS81 to chromatin and thus ensuring the stability of CFSs.

UBE2T promotes the resolution of R-loops located in the promoters of the large genes associated with CFSs

Most CFSs co-localize with very large genes greater than 300 kb [21]. It has been reported that transcription of these large genes extends for more than one cell cycle, which often induces the formation of R-loops and hinders RF progression [46]. Given that UBE2T deficiency caused genome wide accumulation of R-loops especially at promoter regions, we hypothesized that CFSs tended to be more sensitive to the increase of R-loops. Although no genome-wide analysis of CFSs has been undertaken in mice, CFSs in both humans and mice are associated with orthologous large genes [47]. In this study, we selected three large genes nested in mouse CFSs, including *Wwox* in Fra8E1 [48], *Immp2l* in Fra12C1 [49], and *Sec8* in Fra6B1 [47]. The S9.6 CUT&Tag assay showed R-loop signals accumulated in the promoter regions of the *Wwox*, *Immp2l*, and *Sec8* genes, and *Ube2t* knockdown significantly increased the R-loop signals in the promoter regions of *Wwox* and *Immp2l* genes (Fig. 9a). We then performed quantitative PCR (qPCR) analysis following CUT&Tag assay (CUT&Tag-qPCR) in the promoter regions of the three genes and found that the sequences within the promoter regions of *Wwox* and *Immp2l* genes were significantly enriched in the *Ube2t* knockdown cells (Fig. 9b). Although *Sec8* showed no statistical difference between *Ube2t* knockdown groups and control group, there was an enrichment trend (Fig. 9b). These findings demonstrate that UBE2T is involved in R-loop resolution in the large genes of CFSs to promote replication of these regions during S phase.

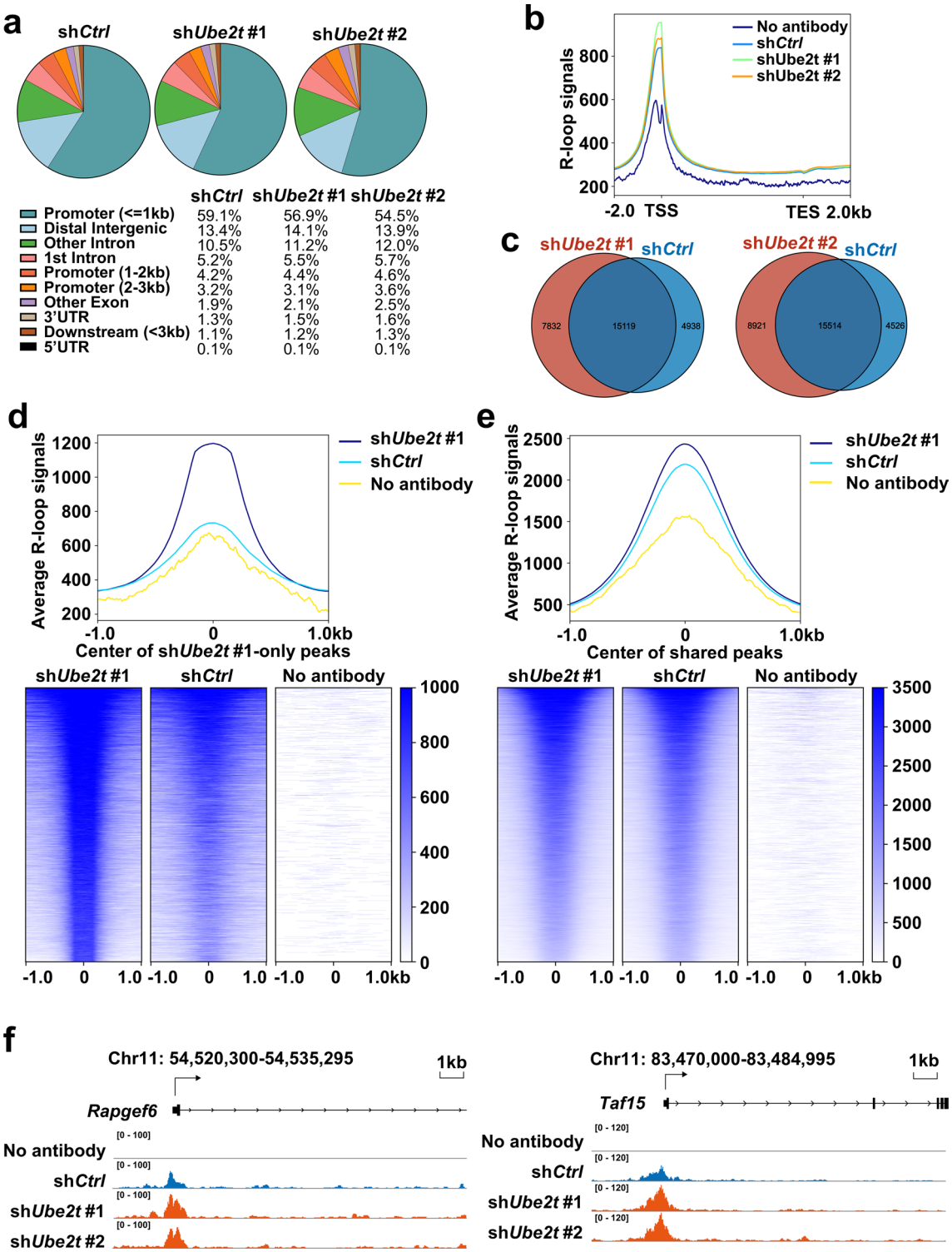

Fig. 5 Knockdown of *Ube2t* causes R-loop accumulation **a** Annotation of R-loop CUT&Tag peaks with pie charts. The genomic distribution of peaks is shown in the low panel. UTR, untranslated region. **b** Genomic metaplots of genes with R-loop signals across the 2 kb window around gene bodies. (**c**) Venn diagrams showing the overlap of R-loop peaks between *Ube2t* knockdown groups (sh*Ube2t* #1, sh*Ube2t* #2) and control group (sh*Ctrl*). **d, e** Average R-loop read density and heatmap of sh*Ube2t* #1 groups, sh*Ctrl* group and no antibody group in the 1 kb window around the center of sh*Ube2t* #1 unique peaks (**d**) and merged peaks (**e**). **f** Genome browser tracks of R-loop coverage at the representative genes *Rapgef6* and *Taf15* in P19 cells. No antibody (green), control (blue), sh*Ube2t* #1 (orange) and sh*Ube2t* #2 (orange) CUT&Tag data are shown

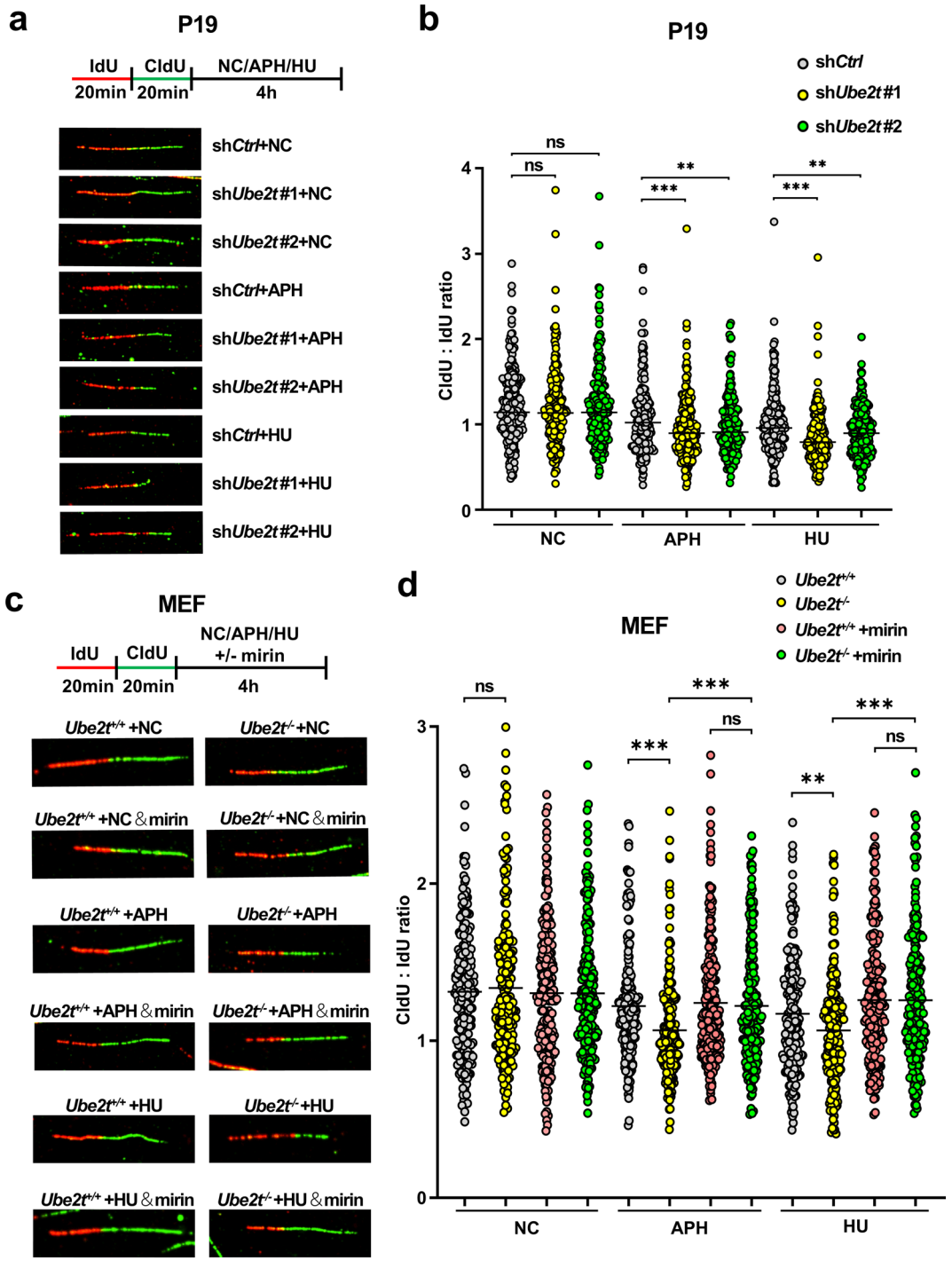

Fig. 6 Loss of UBE2T leads to increased resection of the nascent DNA in P19 cells and MEFs **a, b** The experimental scheme, representative images (**a**) and the CldU/IdU track length (**b**) in the DNA fiber assay in P19 cells infected with sh*Ctrl*, sh*Ube2t* #1, or sh*Ube2t* #2 adenovirus after control, APH (0.2 μM), or HU (0.3 mM) treatment. At least 200 CldU/IdU ratios were included per group, ns: not significant, $^{**}P<0.01$, $^{***}P<0.001$. **c, d** The experimental scheme, representative images (**c**) and the CldU/IdU track length (**d**) of the DNA fiber assay in wild-type and $Ube2t^{-/-}$ MEFs after control, APH (0.2 μM), or HU (0.3 mM) treatment with or without mirin. At least 200 CldU/IdU ratios were included per group. ns: not significant, $^{**}P<0.01$, $^{***}P<0.001$. Data from DNA fibers are presented as dots and the mean values are presented (**b, d**)

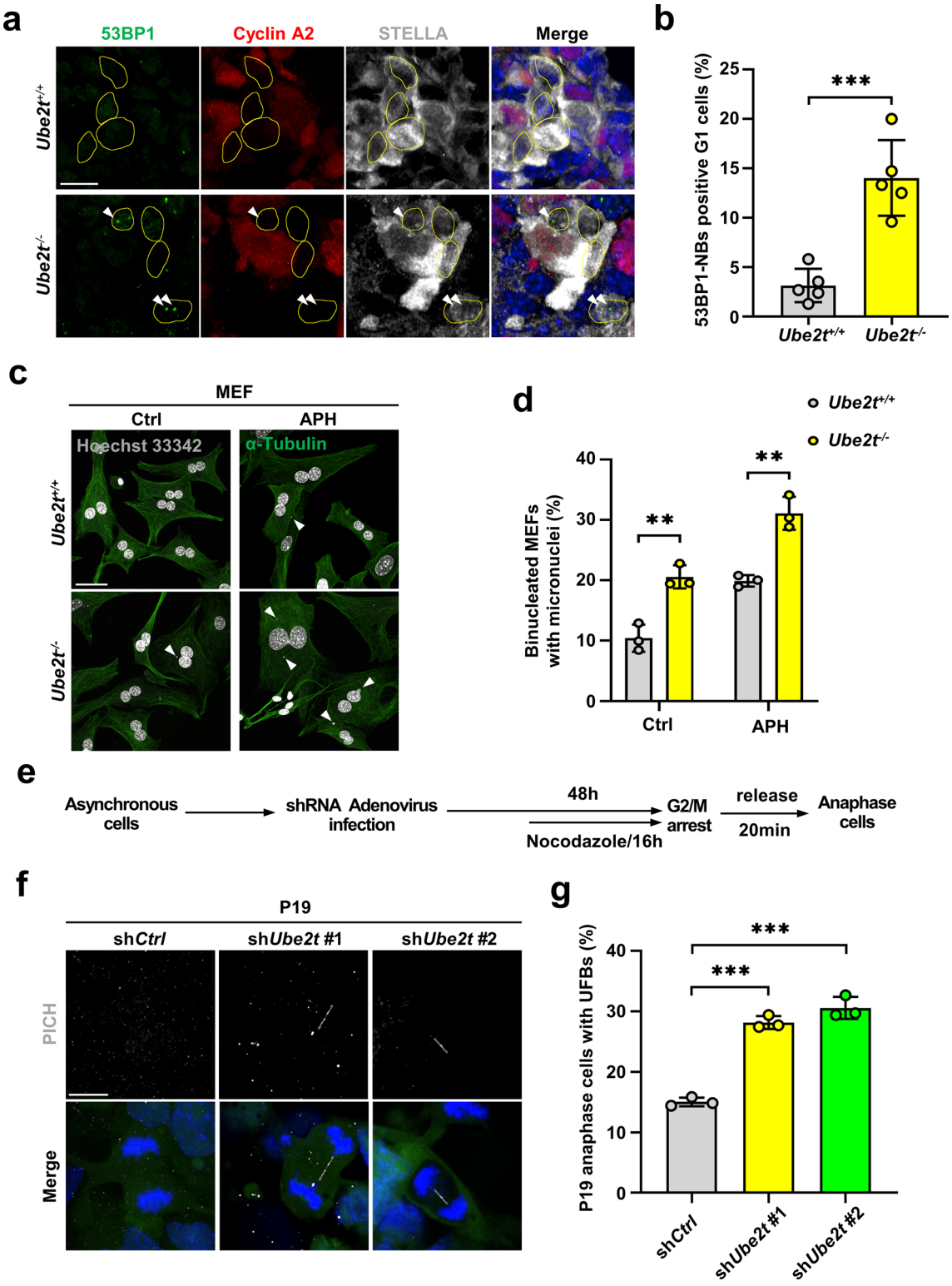

Discussion

In this study, we demonstrate the role of UBE2T in PGCs relating to both TRCs and CFSs and propose a model whereby UBE2T maintains PGC development through multiple mechanisms (Fig. 10). On the one hand, UBE2T is required to activate the FA pathway to counteract TRCs by resolving R-loops and stabilizing RFs. On the other hand, the activated FA pathway protects CFSs by resolving R-loops in large genes and facilitating MiDAS (Fig. 10). When UBE2T

◂**Fig. 7** UBE2T is essential for protecting the stability of CFSs **a, b** Representative images (**a**) and percentages (**b**) of 53BP1-NBs in G1-phase PGCs (STELLA-positive) in E11.5 wild-type and *Ube2t*$^{-/-}$ genital ridges. Large 53BP1 foci (green) indicate 53BP1-NBs. Cyclin A2-negative (red) and STELLA-positive indicate G1-phase PGCs. The nuclei of G1-phase PGCs are circled out. Arrowheads indicate 53BP1-NBs in PGCs. $n=5$ embryos per genotype, $^{***}P<0.001$. Scale bar = 10 µm. **c, d** Representative images (**c**) and percentages (**d**) of binucleated cells with micronuclei in wild-type and *Ube2t*$^{-/-}$ MEFs after APH (0.5 µM) or control treatment. DNA was stained with Hoechst 33342 (white), and α-Tubulin (green) indicates the binucleated MEFs. Arrowheads indicate micronuclei in MEFs. Three biological replicates were performed in each group and at least 200 binucleated MEFs were included per replicate, $^{**}P<0.01$. Scale bar = 200 µm. **e** Experimental workflow for analyzing P19 cells in anaphase following UBE2T depletion. **f, g** Representative images (**f**) and percentages (**g**) of UFB-positive P19 anaphase cells following UBE2T depletion. PICH (white) indicates UFBs, and DNA was stained with Hoechst 33342 (blue). Three biological replicates were performed in each group and at least 100 P19 anaphase cells were included per replicate, $^{***}P<0.001$. Scale bar = 10 µm. Data points from individual embryos (**b**) or groups (**d, g**) are presented as dots, mean ± SD are presented (**b, d, g**)

is absent in PGCs, TRC-related and CFS-related DNA damage accumulates, leading to the activation of the p53 pathway and inhibition of cell proliferation, ultimately resulting in PGC loss and subsequent germ cell exhaustion in mice.

In mouse embryos, following specification, PGCs migrate to the genital ridge and undergo subsequent rapid proliferation up to E13.5 [50]. Later, the female germ cells enter into meiosis and are arrested at the diplotene stage of prophase I while male germ cells undergo mitotic arrest [50]. The maximum of PGC population established by mitosis determines the reproductive reserve of both female and male mammals [1, 51]. Abnormalities in any of aforementioned processes may cause germ cell loss after birth. Several previous studies have reported that the FA proteins are indispensable for rapid proliferation process of PGCs [52–54]. Here we show that UBE2T, a key protein in FA pathway activation, is also crucial for PGC proliferation. After UBE2T deletion in mice, PGCs exhibit obvious proliferation defects and their numbers decrease dramatically. These findings further reinforce the role of the FA pathway in the development of PGCs and provide new mechanistic explanation for the FA-associated infertility.

Germ cells pass on genetic information to the next generation and thus must be equipped with superior capacity of maintaining their genome stability. The FA pathway is a classical DDR pathway, and its inactivation affects PGC proliferation by increasing genome instability that is a shared phenotype in mouse strains with different genetic backgrounds, indicating that this pathway is responsible for resolving specific intrinsic genome threats in PGCs. The characteristics of PGCs, including global decrease in DNA methylation, rapid proliferation, high level of transcription and active metabolism [39, 40, 55, 56], may be the cause of these intrinsic threats. A previous study showed that ERCC1 and FANCA deletion in mice both increased DNA damage in PGCs, and *Aldh2*$^{-/-}$*Fanca*$^{-/-}$ or *Adh5*$^{-/-}$*Fanca*$^{-/-}$ embryos showed fewer PGCs compared to the *Fanca*$^{-/-}$ embryos, suggesting that DNA damage occurred due to the inability of these mice repairing ICLs generated by metabolically-produced aldehydes [7]. Another study found that the de-repression of transposable elements contributed to proliferation defects and DNA damage accumulation in *Fancd2*$^{-/-}$ PGCs [57]. Interestingly, human and murine cells defective in FANCD2 or FANCA show the accumulation of R-loops and DNA damage [18], and the FA pathway resolves conflicts between the replication and transcription machineries [19]. In this study, we show that replication stress from TRCs is an important source of DNA damage in *Ube2t*$^{-/-}$ PGCs, and this provides evidence into the mechanism through which FA pathway inactivation leads to PGC loss.

In addition to TRCs, CFS is regarded as another endogenous source of replication stress and its stability has long been known to be under the control of a large number of proteins that are involved in DNA damage repair and replication stress response [22, 23]. Under-replicated CFSs enter mitosis and undergo MiDAS [25]. It has been suggested that FANCD2 promotes MiDAS [31], and ID2 foci have been observed at the tips of CFS-related UFBs to play roles in UFB resolution [28, 44]. Although the FA pathway has been involved in MiDAS which is different from the RAD52-mediated pathway, the precise mechanism is not clear [31]. It is known that ubiquitylated FANCD2 recruits the nuclease scaffold protein SLX4, which in turn recruits XPF-ERCC1, MUS81-EME1, and SLX1 to chromatin in the classical ICL repair pathway [8]. Similarly, the recruitment of MUS81-EME1 to CFS loci during MiDAS has been shown [45], and deletion of MUS81 has been shown to reduce the occurrence of breaks or gaps in CFSs in metaphase chromosomes [27, 58], but it is still unknown whether the recruitment of the MUS81 endonuclease is related to the FA pathway. In the present study, we show that UBE2T participates in MiDAS to prevent CFS-related DNA damage in PGCs and provide the first evidence that the activated FA pathway recruits MUS81 to chromatin to facilitate MiDAS.

It is well known that CFS-induced delay in the completion of replication in S phase is correlated with initiation paucity [22]. In addition, R-loops usually accumulate at large genes nested in CFS loci [21, 22]. Therefore, it is conceivable that the R-loops may hinder the progress of the RF in the CFS loci, which will further increase the DNA damage in FA pathway-defective cells. In this study, S9.6 CUT&Tag results showed that R-loops were enriched at TSSs and promoter regions, similar to what was reported in a previous study [59]. We confirmed that upon FA pathway inactivation the promoter regions of *Wwox* in Fra8E1and *Immp2l* in Fra12C1 showed R-loop accumulation, which

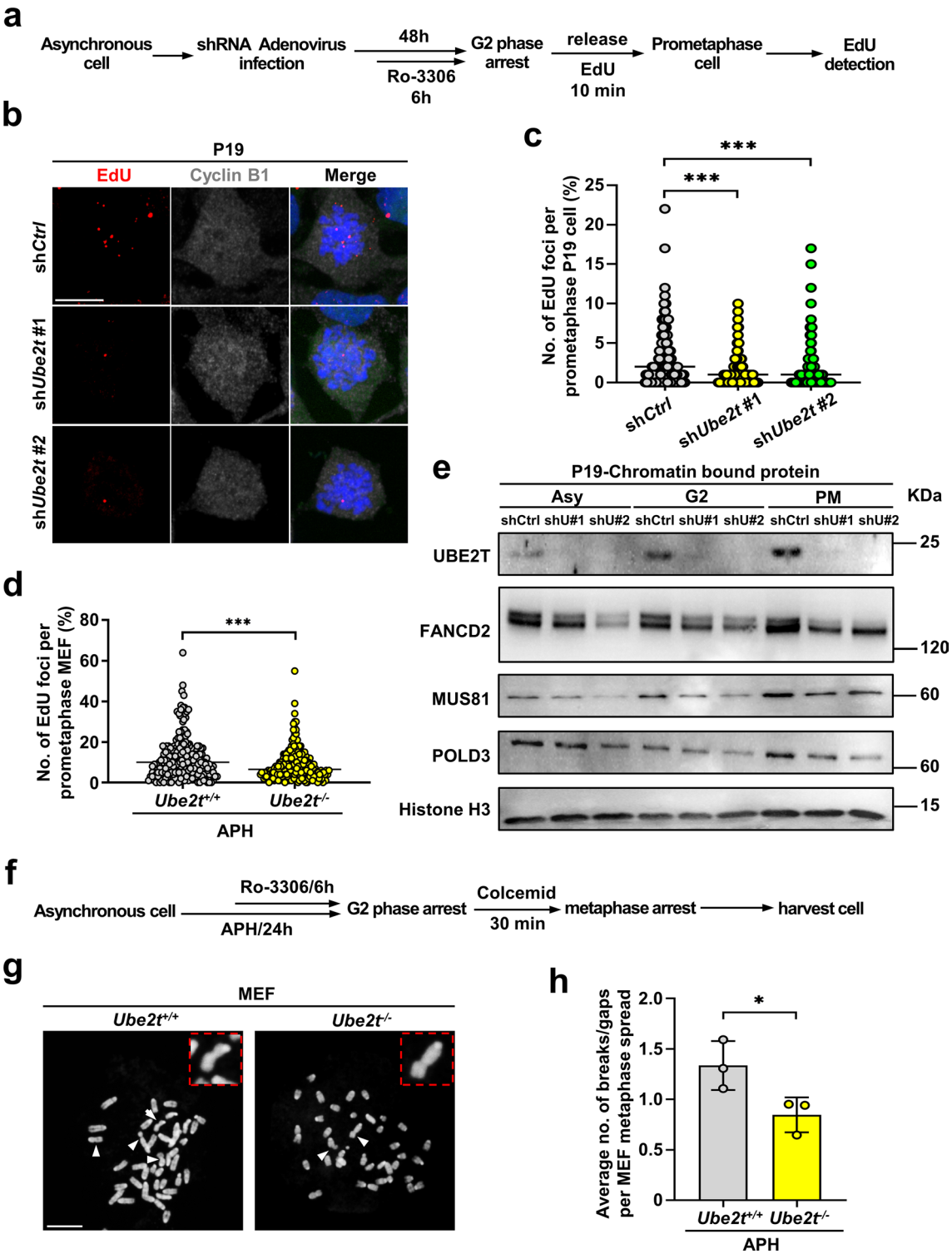

might hinder the RFs in S phase and induce DNA damage. This suggests an additional mechanism through which the FA pathway can protect CFSs by resolving R-loops therein.

In conclusion, we found that UBE2T kept the rapid proliferation of mouse PGCs by counteracting TRCs and maintaining CFS stability, thus assuring the establishment of reproductive reserve. This study thus provides new insights into the infertility phenotype in FA-null mice and FA patients and into the endogenous mechanisms that maintain genome stability in PGCs.

◂**Fig. 8** UBE2T promotes MiDAS by recruiting MUS81 to chromatin **a** Experimental workflow for analyzing MiDAS in P19 prometaphase cells following UBE2T depletion. **b, c** Representative immunofluorescence images (**b**) and quantification (**c**) of MiDAS foci (labeled with EdU; red) in P19 prometaphase cells following UBE2T deletion. Cyclin B1-positive nuclei indicate cells entering mitosis. DNA was stained with Hoechst 33342 (blue). At least 200 P19 prometaphase cells were included per group, $***P < 0.001$. Scale bar = 10 μm. **d** Quantification of MiDAS foci in wild-type and *Ube2t*$^{-/-}$ prometaphase MEFs following APH (0.2 μM) treatment. At least 200 prometaphase MEFs were included per genotype, $***P < 0.001$. **e** Representative western blots of the chromatin-bound fraction of P19 cells at the indicated cell cycle phases for UBE2T, FANCD2, MUS81, POLD3, and Histone H3 (the loading control). Asy, asynchronous; G2, G2 phase; PM, prometaphase; shU#1, sh*Ube2t* #1; shU#2, sh*Ube2t* #2. **f** Experimental workflow for analyzing metaphase MEFs following APH (0.2 μM) treatment. **g** Representative images of metaphase chromosomes of wild-type and *Ube2t*$^{-/-}$ MEF cells after APH (0.2 μM) treatment. DNA was stained with Hoechst 33342 (white). Arrowheads indicate breaks or gaps in the chromosomes. Magnified images of chromosomes are shown in the red squares. Scale bar = 10 μm. **h** Quantification of breaks/gaps per metaphase spread from wild-type and *Ube2t*$^{-/-}$ MEFs following APH (0.2 μM) treatment. Three biological replicates were performed in each group and at least 100 metaphase MEFs were included per replicate. $*P < 0.05$. Data from individual cells (**c, d**) or groups (**h**) are presented as dots, mean (**c, d**) or mean ± SD (**h**) are presented

Materials and methods

Animals

Ube2t$^{-/-}$ and *p53*$^{-/-}$ mice were obtained from Cyagen Bioscience (China) using the CRISPR/Cas9 technology. *Ube2t*$^{-/-}$ mice were generated by targeted deletion of exon 3 to exon 6, which led to a frameshift and truncated protein (Fig. S1a). The *p53*$^{-/-}$ mice were generated by targeted deletion of exon 3 to exon 9. All mice established by the CRISPR/Cas9 technology were derived from C57BL/6 J mice and then crossed with ICR mice. The primer sequences used for genotyping are listed in Table S1. All animal experiments were conducted in accordance with the ethical guidelines approved by the Animal Care and Research Committee of Shandong University.

Cell lines and cell culture

P19 cells were obtained from the Cell Resource Center, IBMS, CAMS/PUMC, China and were cultured in α-MEM with 10% FBS and 1% streptomycin/penicillin. Wild-type and *Ube2t*$^{-/-}$ MEFs were produced using the established methods. In detail, pregnant mice were sacrificed at E12.5 ~ E13.5, the embryos were collected, and a portion of the tissue was removed from each embryo for genotyping. The limbs, tail, head, and viscera of each embryo were carefully removed, and the trunks were minced with sharp scissors. The minced tissues were added to 0.05% trypsin (Invitrogen, China) and digested at 37 °C for 4 min to dissociate into a single cell suspension. MEFs were cultured in DMEM with 10% FBS and 1% streptomycin/penicillin.

Cell synchronization and treatment

To obtain G2-phase cells, cells were synchronized to G2 phase using the CDK1 inhibitor RO-3306 (8 μM; APExBIO, USA; A8885) for 6 h. To obtain prometaphase cells, cells arrested in G2 phase were released into medium and cultured for 10 min. Prometaphase cells were obtained by mitotic shake-off for subcellular fractionation. For MiDAS, cells arrested in G2 phase were then released into medium containing 5-ethynyl-2'-deoxyuridine (EdU; 20 μM; Sigma, China; 900584) and cultured for 10 min to release them to prometaphase. These cells were then fixed for immunofluorescence analysis. To obtain metaphase chromosomes, cells arrested in G2 phase were released into medium containing colcemid (200 ng/ml; Sangon Biotech, China; A606585) for 30 min. Metaphase cells were obtained by mitotic shake-off for metaphase chromosome spreads. To obtain anaphase cells, asynchronous cells were treated with nocodazole (40 ng/ml; Sigma, China; M1404) for 16 h to arrest the cells at G2/M phase. The arrested cells were then released into medium and cultured for 20 min to release them into anaphase. To obtain the binucleated MEFs, asynchronous MEFs were treated with cytochalasin B (1 μg/ml; Sangon Biotech, China; A606580) for 24 h.

Mitomycin C (MMC; TCI, China; M2320) was used for inducing ICLs. Aphidicolin (APH; Sigma, China; 504744) was used for inducing replication stress or CFS-related genome instability. Hydroxyurea (HU; Sigma, China; H8627) was used for inducing replication stress.

Protein extraction and western blot analysis

Total protein was extracted from the testes with the Total Protein Extraction Kit (Invent, China; SD-001), and the protein concentration was determined by the BCA method (ThermoFisher, China). Chromatin-bound protein from P19 cells was fractionated using the Subcellular Protein Fractionation Kit (ThermoFisher, China; 78840), and the BCA method was also used for determining the protein concentration.

For western blot analysis, protein samples were run on an SDS–PAGE gel and then transferred to a PVDF membrane (Millipore, China). Following blocked with 5% milk for 1 h at room temperature, the membrane was incubated overnight with the primary antibody (Table S3) at 4 °C. The membrane was then incubated with the appropriate secondary antibody for 1 h at room temperature, and was developed with an ECL system (Millipore, China). The images were captured by a ChemiDoc MP System (Bio-Rad, China).

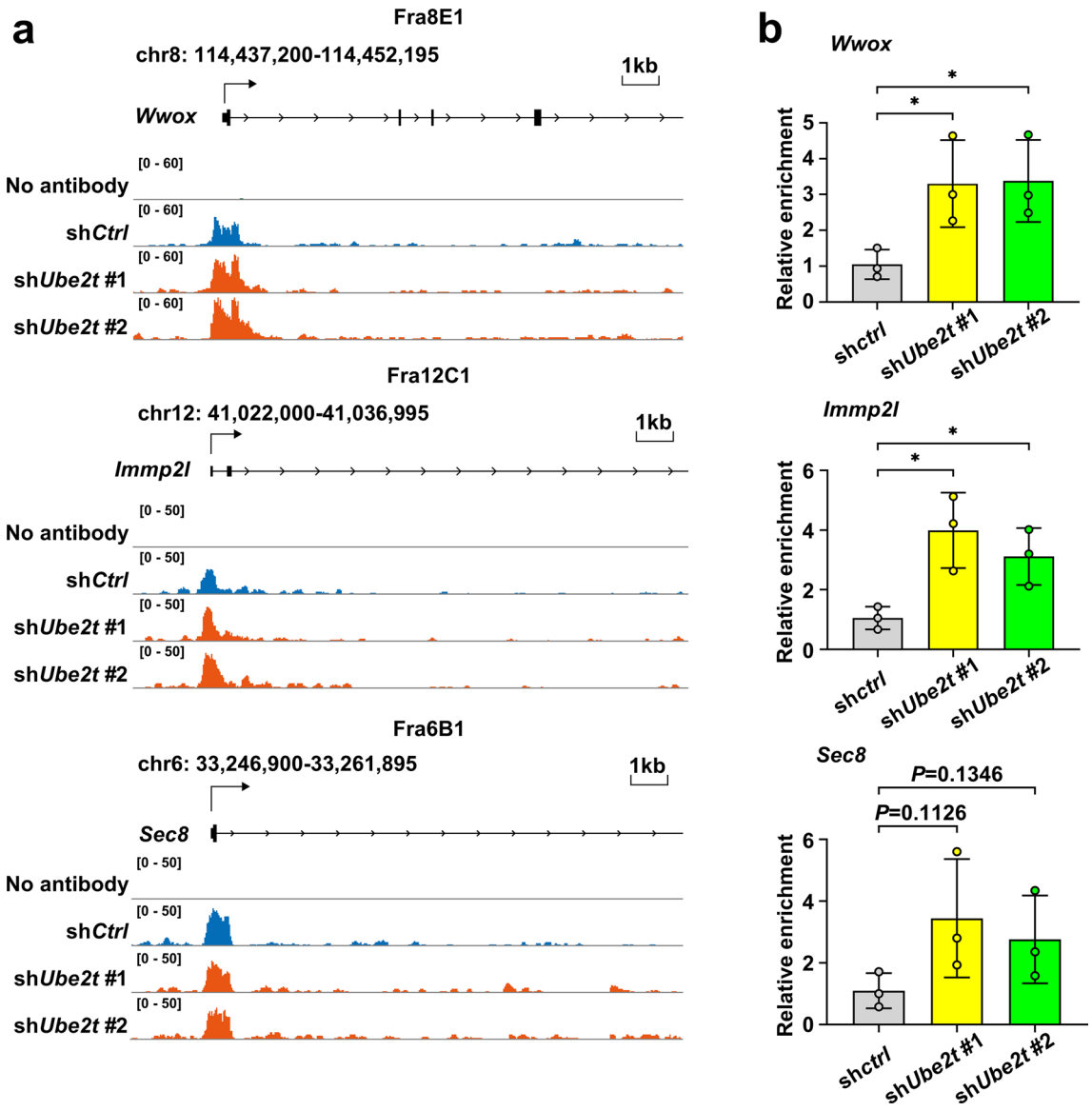

Fig. 9 UBE2T promotes the resolution of R-loops located at CFSs **a** Genome browser tracks of R-loop coverage at the large *Wwox*, *Immp2l*, and *Sec8* loci detected by S9.6 antibody CUT&Tag assay in P19 cells. No antibody (green), control (blue), sh*Ube2t* #1 (orange) and sh*Ube2t* #2 (orange) CUT&Tag data are shown. **b** Quantification of R-loops by CUT&Tag-qPCR at promoter regions of the large genes *Wwox*, *Immp2l*, and *Sec8*. Data points from individual groups are presented as dots, mean ± SD are presented. Three biological replicates were performed in each group. ns: not significant, $^*P < 0.05$

Histological staining

The embryonic gonads were fixed in 4% PFA overnight at 4℃ and washed in PBS three times. The gonads of mice after birth were fixed in Bouin's solution overnight at 4℃ and washed in 70% ethanol three times. Fixed samples were dehydrated with graded alcohol, embedded in paraffin, and sectioned at 5 μm thickness. The samples were deparaffinized, rehydrated, and then stained with hematoxylin and eosin (H&E) using standard methods. Images were captured with an Olympus microscope (BX53, Japan).

For immunohistochemical staining, sections of paraffin-embedded samples were deparaffinized, rehydrated, and boiled with antigen retrieval buffer (10 mM sodium citrate, pH 6.0) for 10 min. Samples were cooled to room temperature and then washed in water for 5 min three times. The samples were blocked and permeabilized with 10% goat or donkey serum diluted in PBS including 0.3% Triton X-100 for 1 h at room temperature. Samples were incubated with the primary antibody (Table S3) diluted in the blocking and permeabilizing buffer at 4 °C overnight. Samples were then washed with PBS containing 0.1% Triton X-100 (PBST)

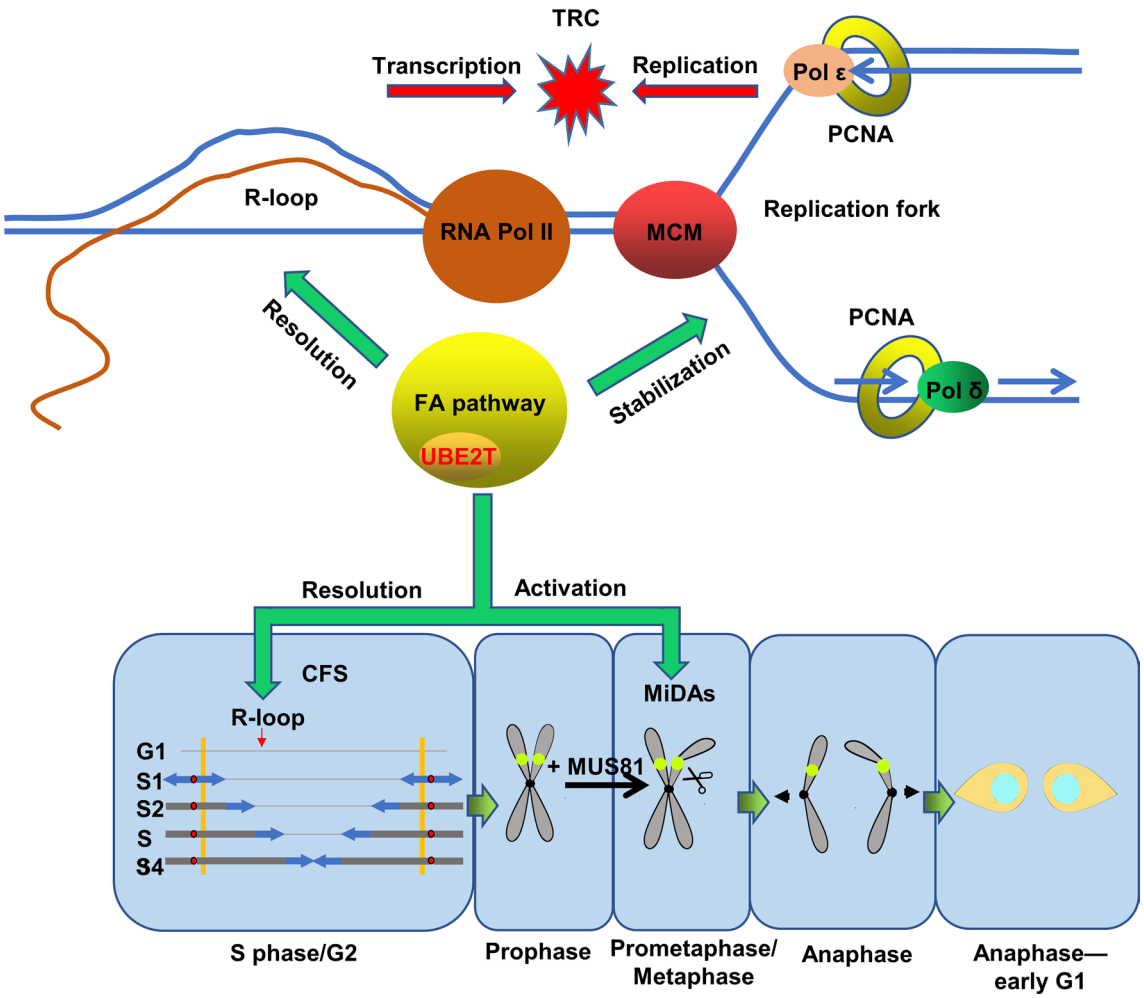

Fig. 10 The working model of how UBE2T maintains genome stability in PGCs. PGCs encounter endogenous replication stress derived from TRCs and CFSs during rapid division. UBE2T is required to activate the FA pathway to resolve R-loops and stabilize RFs to counteract TRCs. The activated FA pathway also resolves R-loops at large genes and facilitates MiDAS to maintain stability of CFSs. Thus, the FA pathway functions to maintain the genome stability of PGCs

three times, and the slides were stained following standard immunohistochemistry methods using a Vectastain ABC Kit (Vector Laboratory, USA). The slides were then counterstained with hematoxylin, dehydrated with an ethanol gradient, and made transparent with xylene. Finally, the samples were mounted and images were captured with an Olympus microscope (BX53, Japan).

For fluorescence staining, samples were treated similarly with traditional immunohistochemical staining methods up to primary antibody treatment. After that, the samples were washed three times with PBST and incubated with the appropriate Alexa Fluor-conjugated secondary antibody diluted in PBST with 5 μg/ml Hoechst 33342 for 1 h at room temperature. Afterwards, the samples were washed three times with PBST and mounted with antifade reagent. Images were captured with a Dragonfly 500 confocal microscope (ANDOR, UK).

Alkaline phosphatase staining

Pregnant mice were sacrificed at E8.5, E9.5, or E11.5, and the embryos were collected and fixed in 4% PFA for 1 h at 4 °C. After washing twice with PBS, the embryos were treated with staining buffer for 20 ~ 30 min on a shaker at 37 °C in the dark. The staining buffer consisted of 25 mM Tris-maleic acid buffer (pH 9.0), 0.5 mM $MgCl_2$, 0.4 mg/ml 1-naphthyl phosphate disodium salt (Sigma, China; N7255), and 1 mg/ml Fast Red TR salt (Sigma, China; F6760). The staining reaction was terminated by adding excessive PBS. After washing twice with ddH_2O, the embryos were made transparent with 40% glycerol and 80% glycerol for 1 h. Images were captured with a stereoscope (Nikon, Japan).

Immunofluorescence analysis

To obtain E11.5 genital ridges, the embryos were fixed in 4% PFA overnight at 4℃ and washed three times in PBS. The genital ridges were dissected and embedded in OCT compound and sectioned at 10 μm. The samples were dipped in PBS to remove the OCT compound and then blocked and permeabilized with 10% bovine serum albumin (BSA) or donkey serum diluted in PBS including 0.3% Triton X-100 for 1 h at room temperature. The primary antibody (Table S3) diluted in blocking and permeabilizing solution was added to incubate at 4℃ overnight. After washing three times with PBST, the samples were incubated with the secondary antibody diluted in PBST with 5 μg/ml Hoechst 33342 for 1 h at room temperature. The samples were washed with PBST three times and mounted with antifade reagent. Images were captured with a Dragonfly 500 confocal microscope (ANDOR, UK).

For both P19 cells and MEFs, the cells were seeded onto gelatin-coated slides, fixed in 4% PFA for 15 min at room temperature, and washed with PBS three times. After transferring to glass slides, the cells were blocked, permeabilized, and incubated with primary antibody and second antibody together with Hoechst 33342 similar to the tissue samples. The images were captured with a Dragonfly 500 confocal microscope (ANDOR, UK).

EdU incorporation assay

Pregnant mice (E11.5) were intraperitoneally injected with a solution containing 100 mg/kg EdU for 1 h. The mice were sacrificed, and frozen sections of the E11.5 genital ridges were obtained as described above. Samples were dipped in PBS to remove the OCT compound and were incubated with 2 mg/ml glycine solution for 10 min, permeabilized with PBS containing 0.5% Triton X-100 for 10 min two times, and incubated with EdU reaction solution (Ribo Bioscience, China; C10371-2) for 30 min at room temperature. The samples were then washed with PBS containing 0.5% Triton X-100 for 10 min and incubated with primary antibody and secondary antibody together with Hoechst 33342 similar to the standard immunofluorescence staining. Images were captured with a Dragonfly 500 confocal microscope (ANDOR, UK).

For both P19 cells and MEFs, the cells were seeded onto gelatin-coated slides and incubated with medium containing 20 μM EdU for 1 h (for the cell cycle assay) or for 10 min (for MiDAS) at 37℃. Cells were fixed with 4% PFA and washed with PBS three times. The fixed cells were then subjected to standard EdU staining and immunofluorescence staining similar to the tissue samples. Images were captured with a Dragonfly 500 confocal microscope (ANDOR, UK).

For cell cycle phase analysis, E11.5 genital ridges were subjected to EdU incorporation assay as above and followed with the immunofluorescence staining of Cyclin B1 and STELLA. P19 cells were performed with EdU incorporation assay as above and followed with the immunofluorescence staining of Cyclin B1. Cyclin B1 negative indicates G1-phase cells; EdU positive indicates S-phase cells; Cyclin B1 strongly positive in cytoplasm indicates G2-phase cells; Cyclin B1 accumulation in the nucleus indicates M-phase cells.

Magnetic PGC sorting

Pregnant mice (E11.5) were sacrificed, and a portion of tissue from the embryos was taken for quick genotyping using the KAPA Mouse Genotyping Kit (Sigma, China; KK7351). The wild-type and *Ube2t*$^{-/-}$ genital ridges were dissected and collected separately in cold Leibovitz's L-15 medium and incubated with Accutase (ThermoFisher, China; A11105-01) for 25 min at 37℃ to dissociate into a single-cell suspensions. The samples were resuspended with 80 μl buffer (DPBS with 0.5% BSA and 2 mM EDTA), and 20 μl anti-SSEA-1 beads were added to the samples. The samples were mixed well and incubated for 15 min at 4℃. One milliliter buffer was added to the wash the samples, and the cells were collected by centrifugation at 300 × *g* for 8 min at 4℃ and resuspended in 500 μl buffer. The separation columns were put on the magnetic stand and rinsed with 500 μl buffer. The cells were added to the separation columns, and the somatic cells (unlabeled cells) were washed out of the columns. The cells left on the columns were washed with 500 μl buffer three times and immediately added to 500 μl buffer. Collection tubes were placed under the columns, and the magnetically labeled SSEA-1-positive PGCs were eluted into the collection tubes by quickly pushing the plunger into the columns. The magnetic-positive cells were collected by centrifugation at 300 × *g* for 8 min at 4 °C and resuspended with cold DPBS at a concentration of 1×10^6 cells/ml for use in the neutral comet assay.

Neutral comet assay

Magnetically sorted PGCs, P19 cells, and MEFs were subjected to a neutral comet assay as described previously [60]. Eighty microliters of melted agarose with a normal melting temperature were spread onto the glass slides, and a coverslip was placed onto the agarose. The slides were kept at 4℃ for 15 min to let the agarose solidify, and the coverslips were removed. Ten microliters of cell suspension diluted in DPBS at a concentration of 1×10^6 cells/ml and 70 μl melted agarose with low melting temperature (Sangon Biotech, China; A600015) were mixed well and added onto the slides with a coverslip. The slides were

kept at 4℃ for 15 min to let the agarose solidify, the coverslips were then removed, and the slides were immersed in a neutral lysis buffer (2.5 M NaCl, 100 mM Na_2EDTA, 10 mM Tris, 1% N-lauroylsarcosine, and 1% Triton X-100 [pH 9.5]) for 1 h at room temperature. The slides were washed with ddH_2O three times and transferred to an electrophoresis tank including neutral electrophoresis solution (300 mM sodium acetate, 100 mM Tris [pH 8.3]). After incubating in neutral electrophoresis solution for 20 min, the samples underwent electrophoresis at 80 mA and 20 V for 20 min. The slides were washed with ddH_2O three times and fixed with 100% ethanol. The air-dried slides were washed with ddH_2O and stained with PBS containing 5 μg/ml Hoechst 33342 for 30 min at room temperature. The samples were mounted with antifade reagent, and the images were captured with an Olympus microscope (BX53, Japan). The OTMs were analyzed by the CASP software (CASPLab).

Proximity ligation assay (PLA)

The PLA staining was performed using Duolink PLA Technology (Sigma, China) as described previously [61]. The genital ridges from E11.5 embryos were blocked, permeabilized, and incubated with the RNA Pol II and PCNA primary antibodies as described for the immunofluorescence assay. The secondary antibody probe incubation, ligation, and amplification reaction were performed according to the manufacturer's instructions. Duolink in situ PLA probe anti-mouse plus (Sigma, China; DUO92001), Duolink in situ PLA probe anti-rabbit minus (Sigma, China; DUO92005), and Duolink in situ Detection Reagents Red (Sigma, China; DUO92008) were used in the PLA staining. After the PLA staining, the slides were incubated with the STELLA antibody overnight at 4℃ and the appropriate secondary antibody for 1 h at room temperature to label PGCs. Finally, the slides were incubated with PBS containing 5 μg/ml Hoechst 33342 for 30 min at room temperature and mounted with antifade reagent. Images were captured with a Dragonfly 500 confocal microscope (ANDOR, UK).

For the PLA in MEFs, cells were seeded onto prewarmed, gelatin-coated slides, fixed with 4% PFA, and washed three times with PBS. The fixed cells were permeabilized with cold methanol for 10 min at –20 °C, washed with ddH_2O three times, and blocked in 10% donkey serum containing 0.3% Triton X-100 for 1 h at room temperature. The cells underwent PLA staining with the RNA Pol II and PCNA antibodies and DNA staining with Hoechst 33342 as described above for the genital ridges. Images were captured with a Dragonfly 500 confocal microscope (ANDOR, UK).

DNA fiber assay

The DNA fiber assay was performed as described previously [62]. P19 cells were pulse-labeled with 500 μM 5-iodo-2'-deoxyuridine (IdU; Sigma, China; I7125) for 20 min, washed with pre-warmed PBS three times, and pulse-labeled with 250 μM 5-chloro-2'-deoxyuridine (CldU; Sigma, China; C6891) for 20 min. MEFs were pulse-labeled with 25 μM IdU for 20 min, washed with pre-warmed PBS three times, and then pulse-labeled with 250 μM CldU for 20 min. The cells were washed with PBS three times and incubated with normal medium or medium with APH or HU for 4 h together with mirin (Selleck, China; S8096) or not. The cells were then digested and resuspended in cold PBS at a concentration of $5\times10^5\sim1\times10^6$ cells/ml. Two microliters of the cell suspension were spotted on one side of the glass slides and air-dried for 3 min. The samples were lysed with 12 μl of lysis buffer (50 mM EDTA and 0.5% SDS in 200 mM Tris–HCl, pH 7.5). The slides were tilted to 15°~45° to spread the DNA fibers and then air-dried completely. The samples were fixed with a mixture of methanol and acetic acid (3:1) and air-dried. After washing twice with ddH_2O, the slides were denatured in 2 N HCl for 1 h at room temperature, washed with PBS three times, and blocked with 1% BSA in PBS for 1 h. The slides were subjected to a standard immunofluorescence procedure with anti-BrdU (rat) and anti-BrdU (mouse) antibodies to label the nascent DNA before mounting with antifade reagent. Images were captured with a Dragonfly 500 confocal microscope (ANDOR, UK). Measurement of the length of IdU and CldU was performed using ImageJ software.

To assess the velocity of the RFs, cells were immediately collected and resuspended in cold PBS after IdU and CldU labeling, and similar DNA fiber assay procedures were performed as described above.

Metaphase chromosome spreads

Metaphase chromosome spreads were performed following an established method [25]. Cells synchronized in metaphase as described above were collected using mitotic shake-off. The cells were pelleted by centrifugation at $600\times g$ for 5 min before being swollen in a pre-warmed 75 mM KCl solution for 5 min at 37℃. The swollen cells were collected by centrifugation at $600\times g$ for 5 min and fixed with a mixture of methanol and acetic acid (3:1). The fixed cells were dropped and spread onto prehydrated glass slides and air-dried at room temperature, washed with PBS three times, incubated with PBS containing 5 μg/ml Hoechst 33,342 for 30 min at room temperature, and mounted with antifade reagent. Images were captured with a Dragonfly 500 confocal microscope (ANDOR, UK).

CUT&tag library generation and high-throughput sequencing

The CUT&Tag assay was performed as previously described [59] with the Hyperactive Universal CUT&Tag Assay Kit for Illumina (Vazyme Biotech, China; TD903). In brief, *Ube2t* knockdown or control P19 cells were washed with washing buffer and then incubated with 10 µl pre-washed ConA beads in a 0.2 ml low-binding 8-strip tube. Fifty microliters of antibody buffer with 1 µg S9.6 antibody was added and incubated overnight at 4℃. The no-antibody control was incubated without primary antibody. Fifty microliters of DIG wash buffer with 0.6 µg secondary antibody was used and incubated for 1 h at room temperature. After washing three times with DIG wash buffer, 100 µl DIG-300 buffer with 2 µl pA/G–Tnp was added and incubated at room temperature for 1 h. The samples were then washed three times with DIG-300 buffer. Fifty microliters of tagmentation buffer were added to the samples and then incubated at 37 °C for 1 h. The reaction was stopped with 5 µl proteinase K, 100 µl buffer L/B and 20 µl DNA extraction beads. The samples were washed once with buffer WA and twice with buffer WB. DNA was extracted in ultrapure water and PCR was performed to amplify the libraries. All libraries were sequenced on an Illumina Novaseq platform according to the manufacturer's instructions.

All CUT&Tag data were mapped to the mm10 genome using BWA v0.7.12. All low-quality reads and PCR adapters were removed. The BamCoverage command from deepTools 3.0.2 was used to generate the track files [63]. All peak calling was performed with MACS2 2.1.2 using the options (macs2 -q 0.05 –call-summits –nomodel –shift -100 –extsize 200 –keep-dup all) [63]. The genomic distribution of CUT&Tag peaks was annotated with the R package ChIPseeker. Heatmaps and metaplots were made for the protein-coding genes or specific peaks using deepTools 3.0.2 [63].

CUT&tag-qPCR analysis

DNA samples for CUT&Tag-qPCR analysis were obtained using the same procedure as for CUT&Tag. The qPCR was performed using a SYBR Premix Ex Taq Reagent Kit (Takara, China). The primer sequences used in this study are presented in Table S2. To calculate the quantitative changes, CT values of the no-antibody samples (N_{CT}) were subtracted from those of the corresponding S9.6 CUT&Tag samples (S_{CT}). The ($S_{CT}-N_{CT}$) value for each sample was then normalized to the ($S_{CT}-N_{CT}$) value obtained from the amplification of DNA samples from P19 cells infected with control adenovirus, and the relative degree of enrichment of the sequences was evaluated by the $2^{-\Delta\Delta CT}$ method.

Statistical analysis

All statistical analyses were performed with SPSS 16.0 software (IBM, USA). GraphPad Prism v8.3.0 was used for graph construction. Two-tailed *P*-values were obtained using Student's *t*-test. $P < 0.05$ was considered to be statistically significant.

Supplementary Information The online version contains supplementary material available at https://doi.org/10.1007/s00018-023-04733-8.

Acknowledgements The authors thank Prof. Ping Zheng from Kunming Institute of Zoology, Chinese Academy of Sciences for providing technical support about DNA fiber assay and comet assay.

Author contributions Shidou Zhao, YQ, and JM designed the study. Y Yu performed most experiments; Y Yang completed the DNA fiber assay; WX completed the neutral comet assay; CW and Simin Zhao helped with the generation of MEFs; GL and RL participated in the genotyping; The manuscript was written by Y Yu and revised by Shidou Zhao, YQ and Z-JC.

Funding This work was supported by the National Key Research and Development Program of China [2022YFC2703800 and 2021YFC2700100]; Basic Science Center Program of NSFC [31988101]; National Natural Science Foundation for Distinguished Young Scholars [82125014]; National Natural Science Foundation of China [32170867 and 82071609]; Natural Science Foundation of Shandong Province for Grand Basic Projects [ZR2021ZD33]; Shandong Provincial Key Research and Development Program [2020ZLYS02]; Research Unit of Gametogenesis and Health of ART-Offspring; Chinese Academy of Medical Sciences [2020RU001]; Taishan Scholars Program for Young Experts of Shandong Province; and Qilu Young Scholars Program of Shandong University.

Data availability The sequencing data are available in Gene Expression Omnibus (GEO) database with the accession number GSE223410 (https://www.ncbi.nlm.nih.gov/geo/query/acc.cgi?acc=GSE223410). Enter token ujexukgqhtiltor into the box to review the data.

Declarations

Conflict of interest The authors declare no competing interests.

Ethical approval All animal experiments were conducted in accordance with the ethical guidelines approved by the Animal Care and Research Committee of Shandong University.

References

1. Findlay JK, Hutt KJ, Hickey M, Anderson RA (2015) How Is the number of primordial follicles in the ovarian reserve established. Biol Reprod 93:111
2. Bolcun-Filas E, Rinaldi VD, White ME, Schimenti JC (2014) Reversal of female infertility by Chk2 ablation reveals the oocyte DNA damage checkpoint pathway. Science 343:533–536
3. Musson R, Gąsior Ł, Bisogno S, Ptak GE (2022) DNA damage in preimplantation embryos and gametes: specification, clinical relevance and repair strategies. Hum Reprod Update 28:376–399

4. Ruth KS, Day FR, Hussain J et al (2021) Genetic insights into biological mechanisms governing human ovarian ageing. Nature 596:393–397
5. Tsui V, Crismani W (2019) The fanconi anemia pathway and fertility. Trends Genet 35:199–214
6. Luo Y, Hartford SA, Zeng R, Southard TL, Shima N, Schimenti JC (2014) Hypersensitivity of primordial germ cells to compromised replication-associated DNA repair involves ATM-p53-p21 signaling. PLoS Genet 10:e1004471
7. Hill RJ, Crossan GP (2019) DNA cross-link repair safeguards genomic stability during premeiotic germ cell development. Nat Genet 51:1283–1294
8. Ceccaldi R, Sarangi P, D'Andrea AD (2016) The fanconi anaemia pathway: new players and new functions. Nat Rev Mol Cell Biol 17:337–349
9. Mamrak NE, Shimamura A, Howlett NG (2017) Recent discoveries in the molecular pathogenesis of the inherited bone marrow failure syndrome fanconi anemia. Blood Rev 31:93–99
10. Howlett NG, Taniguchi T, Durkin SG, D'Andrea AD, Glover TW (2005) The fanconi anemia pathway is required for the DNA replication stress response and for the regulation of common fragile site stability. Hum Mol Genet 14:693–701
11. Luebben SW, Kawabata T, Johnson CS, O'Sullivan MG, Shima N (2014) A concomitant loss of dormant origins and FANCC exacerbates genome instability by impairing DNA replication fork progression. Nucleic Acids Res 42:5605–5615
12. Schlacher K, Christ N, Siaud N, Egashira A, Wu H, Jasin M (2011) Double-strand break repair-independent role for BRCA2 in blocking stalled replication fork degradation by MRE11. Cell 145:529–542
13. Schlacher K, Wu H, Jasin M (2012) A distinct replication fork protection pathway connects fanconi anemia tumor suppressors to RAD51-BRCA1/2. Cancer Cell 22:106–116
14. Gómez-González B, Aguilera A (2019) Transcription-mediated replication hindrance: a major driver of genome instability. Genes Dev 33:1008–1026
15. Roques C, Coulombe Y, Delannoy M et al (2009) MRE11-RAD50-NBS1 is a critical regulator of FANCD2 stability and function during DNA double-strand break repair. EMBO J 28:2400–2413
16. Yeo JE, Lee EH, Hendrickson EA, Sobeck A (2014) CtIP mediates replication fork recovery in a FANCD2-regulated manner. Hum Mol Genet 23:3695–3705
17. García-Muse T, Aguilera A (2016) Transcription-replication conflicts: how they occur and how they are resolved. Nat Rev Mol Cell Biol 17:553–563
18. García-Rubio ML, Pérez-Calero C, Barroso SI et al (2015) The fanconi anemia pathway protects genome integrity from R-loops. PLoS Genet 11:e1005674
19. Schwab RA, Nieminuszczy J, Shah F et al (2015) The fanconi anemia pathway maintains genome stability by coordinating replication and transcription. Mol Cell 60:351–361
20. Li S, Wu X (2020) Common fragile sites: protection and repair. Cell Biosci 10:29
21. Le TB, Millot GA, Blin ME, Brison O, Dutrillaux B, Debatisse M (2013) Common fragile site profiling in epithelial and erythroid cells reveals that most recurrent cancer deletions lie in fragile sites hosting large genes. Cell Rep 4:420–428
22. Debatisse M, Le TB, Letessier A, Dutrillaux B, Brison O (2012) Common fragile sites: mechanisms of instability revisited. Trends Genet 28:22–32
23. Zeman MK, Cimprich KA (2014) Causes and consequences of replication stress. Nat Cell Biol 16:2–9
24. El AE, Gerbault-Seureau M, Muleris M, Dutrillaux B, Debatisse M (2005) Premature condensation induces breaks at the interface of early and late replicating chromosome bands bearing common fragile sites. Proc Natl Acad Sci U S A 102:18069–18074
25. Minocherhomji S, Ying S, Bjerregaard VA et al (2015) Replication stress activates DNA repair synthesis in mitosis. Nature 528:286–290
26. Bhowmick R, Minocherhomji S, Hickson ID (2016) RAD52 facilitates mitotic DNA synthesis following replication stress. Mol Cell 64:1117–1126
27. Naim V, Wilhelm T, Debatisse M, Rosselli F (2013) ERCC1 and MUS81-EME1 promote sister chromatid separation by processing late replication intermediates at common fragile sites during mitosis. Nat Cell Biol 15:1008–1015
28. Chan KL, Palmai-Pallag T, Ying S, Hickson ID (2009) Replication stress induces sister-chromatid bridging at fragile site loci in mitosis. Nat Cell Biol 11:753–760
29. Harrigan JA, Belotserkovskaya R, Coates J et al (2011) Replication stress induces 53BP1-containing OPT domains in G1 cells. J Cell Biol 193:97–108
30. Lukas C, Savic V, Bekker-Jensen S et al (2011) 53BP1 nuclear bodies form around DNA lesions generated by mitotic transmission of chromosomes under replication stress. Nat Cell Biol 13:243–253
31. Graber-Feesl CL, Pederson KD, Aney KJ, Shima N (2019) Mitotic DNA synthesis is differentially regulated between cancer and non-cancerous cells. Mol Cancer Res 17:1687–1698
32. Alpi A, Langevin F, Mosedale G, Machida YJ, Dutta A, Patel KJ (2007) UBE2T, the fanconi anemia core complex, and FANCD2 are recruited independently to chromatin: a basis for the regulation of FANCD2 monoubiquitination. Mol Cell Biol 27:8421–8430
33. Lewis TW, Barthelemy JR, Virts EL et al (2019) Deficiency of the Fanconi anemia E2 ubiqitin conjugase UBE2T only partially abrogates Alu-mediated recombination in a new model of homology dependent recombination. Nucleic Acids Res 47:3503–3520
34. Spiller CM, Bowles J, Koopman P (2012) Regulation of germ cell meiosis in the fetal ovary. Int J Dev Biol 56:779–787
35. Vanni VS, Campo G, Cioffi R et al (2022) The neglected members of the family: non-BRCA mutations in the fanconi anemia/BRCA pathway and reproduction. Hum Reprod Update 28:296–311
36. Bremer S, Vogel R (1999) Pluripotent stem cells of the mouse as a potential in vitro model for mammalian germ cells. Sister chromatid exchanges induced by MMC and ENU in undifferentiated cell lines compared to differentiated cell lines. Mutat Res 444:97–102
37. Fischer M (2017) Census and evaluation of p53 target genes. Oncogene 36:3943–3956
38. Ceccaldi R, Parmar K, Mouly E et al (2012) Bone marrow failure in Fanconi anemia is triggered by an exacerbated p53/p21 DNA damage response that impairs hematopoietic stem and progenitor cells. Cell Stem Cell 11:36–49
39. Kagiwada S, Kurimoto K, Hirota T, Yamaji M, Saitou M (2013) Replication-coupled passive DNA demethylation for the erasure of genome imprints in mice. EMBO J 32:340–353
40. Seki Y, Yamaji M, Yabuta Y et al (2007) Cellular dynamics associated with the genome-wide epigenetic reprogramming in migrating primordial germ cells in mice. Development 134:2627–2638
41. García-Rubio M, Aguilera P, Lafuente-Barquero J et al (2018) Yra1-bound RNA-DNA hybrids cause orientation-independent transcription-replication collisions and telomere instability. Genes Dev 32:965–977
42. Aguilera A, García-Muse T (2012) R loops: from transcription byproducts to threats to genome stability. Mol Cell 46:115–124
43. Gan W, Guan Z, Liu J et al (2011) R-loop-mediated genomic instability is caused by impairment of replication fork progression. Genes Dev 25:2041–2056
44. Naim V, Rosselli F (2009) The FANC pathway and BLM collaborate during mitosis to prevent micro-nucleation and chromosome abnormalities. Nat Cell Biol 11:761–768

45. Minocherhomji S, Hickson ID (2014) Structure-specific endonucleases: guardians of fragile site stability. Trends Cell Biol 24:321–327
46. Helmrich A, Ballarino M, Tora L (2011) Collisions between replication and transcription complexes cause common fragile site instability at the longest human genes. Mol Cell 44:966–977
47. Helmrich A, Stout-Weider K, Hermann K, Schrock E, Heiden T (2006) Common fragile sites are conserved features of human and mouse chromosomes and relate to large active genes. Genome Res 16:1222–1230
48. Krummel KA, Denison SR, Calhoun E, Phillips LA, Smith DI (2002) The common fragile site FRA16D and its associated gene WWOX are highly conserved in the mouse at Fra8E1. Genes Chromosomes Cancer 34:154–167
49. Helmrich A, Stout-Weider K, Matthaei A, Hermann K, Heiden T, Schrock E (2007) Identification of the human/mouse syntenic common fragile site FRA7K/Fra12C1–relation of FRA7K and other human common fragile sites on chromosome 7 to evolutionary breakpoints. Int J Cancer 120:48–54
50. Saitou M, Miyauchi H (2016) Gametogenesis from pluripotent stem cells. Cell Stem Cell 18:721–735
51. Tan H, Tee WW (2019) Committing the primordial germ cell: an updated molecular perspective. Wiley Interdiscip Rev Syst Biol Med 11:e1436
52. Holloway JK, Mohan S, Balmus G et al (2011) Mammalian BTBD12 (SLX4) protects against genomic instability during mammalian spermatogenesis. PLoS Genet 7:e1002094
53. Nadler JJ, Braun RE (2000) Fanconi anemia complementation group C is required for proliferation of murine primordial germ cells. Genesis 27:117–123
54. Wong JC, Alon N, Mckerlie C, Huang JR, Meyn MS, Buchwald M (2003) Targeted disruption of exons 1 to 6 of the fanconi anemia group a gene leads to growth retardation, strain-specific microphthalmia, meiotic defects and primordial germ cell hypoplasia. Hum Mol Genet 12:2063–2076
55. Hayashi Y, Otsuka K, Ebina M et al (2017) Distinct requirements for energy metabolism in mouse primordial germ cells and their reprogramming to embryonic germ cells. Proc Natl Acad Sci U S A 114:8289–8294
56. Leitch HG, Tang WW, Surani MA (2013) Primordial germ-cell development and epigenetic reprogramming in mammals. Curr Top Dev Biol 104:149–187
57. Nie Y, Wilson AF, DeFalco T, Meetei AR, Namekawa SH, Pang Q (2020) FANCD2 is required for the repression of germline transposable elements. Reproduction 159:659–668
58. Ying S, Minocherhomji S, Chan KL et al (2013) MUS81 promotes common fragile site expression. Nat Cell Biol 15:1001–1007
59. Wang K, Wang H, Li C et al (2021) Genomic profiling of native R loops with a DNA-RNA hybrid recognition sensor. Sci Adv. 7:eabe3516
60. Swain U, Subba RK (2011) Study of DNA damage via the comet assay and base excision repair activities in rat brain neurons and astrocytes during aging. Mech Ageing Dev 132:374–381
61. Bayona-Feliu A, Barroso S, Muñoz S, Aguilera A (2021) The SWI/SNF chromatin remodeling complex helps resolve R-loop-mediated transcription-replication conflicts. Nat Genet 53:1050–1063
62. Schwab RA, Niedzwiedz W (2011) Visualization of DNA replication in the vertebrate model system DT40 using the DNA fiber technique. J Vis Exp. https://doi.org/10.3791/3255
63. Ramírez F, Dündar F, Diehl S, Grüning BA, Manke T (2014) deepTools: a flexible platform for exploring deep-sequencing data. Nucleic Acids Res 42:W187-191